Thesis for the degree of Doctor of Philosophy in Thermo and Fluid Dynamics

Experimental Aerothermal Study of Internal Jet Engine Structures

Isak Jonsson

Department of Mechanics and Maritime Sciences
CHALMERS UNIVERSITY OF TECHNOLOGY
Göteborg, Sweden 2021

Experimental Aerothermal Study of Internal Jet Engine Structures
Isak Jonsson
978-91-7905-582-0

Doktorsavhandlingar vid Chalmers tekniska högskola
Ny serie nr 2021:5049

Department of Mechanics and Maritime Sciences
Chalmers University of Technology
SE–412 96 Göteborg, Sweden
Telephone + 46 (0) 31 – 772 5079

Cover: Surface temperature on the suction side of an outlet guide vane in a turbine rear structure.

Typeset by the author using LaTeX.

Printed by Chalmers Reproservice
Göteborg, Sweden 2021

"Design is an iterative process. The necessary number of iterations is one more than the number you have currently done. This is true at any point in time." - Akin's Laws of Spacecraft Design

Abstract

Experimental Aerothermal Study of Internal Jet Engine Structures
Thesis for the degree of Doctor of Philosophy in Thermo and Fluid Dynamics
ISAK JONSSON
Department of Mechanics and Maritime Sciences Division of Fluid Dynamics
Chalmers University of Technology

In commercial aviation, efficiency improvements may be gained by aerodynamic optimisation of its structural components, such as the intermediate compressor duct (ICD) and the turbine rear structure (TRS). These components have frequently been overlooked in favour of compressor and turbine module optimisation. This means that publicly available information on these structural components is relatively sparse, even though such components may offer substantial weight reduction and, with the introduction of hydrogen as aviation fuel, novel synergistic component integration.

This thesis presents heuristic solutions to meet modern demands for verification data on two commercial aviation engine components, the ICD and TRS. The work spans separate research projects and addresses both method development and test facility design.

The development of two measurement methods is presented. First, detailed uncertainty analysis of multi-hole probe implementation in the TRS has led to a 50% reduction in uncertainty regarding total pressure measurement. Furthermore, a modern approach to measuring convective heat transfer has been developed and implemented on the outlet guide vane in the TRS. Neither of the two approaches presented here is limited to applications in the TRS or ICD and may be used in other applications. The aerothermal performance of the TRS for two different Reynolds numbers, several flow coefficients and three different surface roughness numbers have been investigated, and novel results on transition location, streamlines, heat transfer and loss distribution are presented. The second part of the thesis describes the design of a new, low speed, 2.5 stage low-pressure compressor (LPC) facility, built to investigate novel concepts of hydrogen integration in the ICD. Methods developed in the TRS are adopted and implemented in the new facility. A pre-study of the LPC and ICD instrumentation shows that compressor performance may be measured with better than 1% uncertainty using gas path studies.

Keywords: aerothermal, experimental, multi-hole probe, IR-thermography, heat transfer, turbine rear structure, laminar-turbulent transition, intermediate compressor duct, hydrogen propulsion, uncertainty analysis

Acknowledgments

As my work in the laboratory has been connected to numerous projects in different fields, I would like to thank too many people to mention for their great company, help and exciting discussions. Therefore, I hereby give my gratitude to all of you. However, some individuals are directly connected to this thesis and cannot be left out with a clean conscience.

The first person is my very knowledgeable supervisor Professor Valery Chernoray who has done his best to steer me away from ill-suited decisions since my first day in the lab many years ago. Thank you to PhD Borja Rojo for enduring me during the intensive but exciting period when finalising the LPT-OGV rig. Furthermore, Tomas Grönsted and Carlos Xisto should also be mentioned for their outstanding support and trust in me in our ongoing venture in ENABLEH2. Finally, I'm honoured to work with such great colleagues and collaborators that are heavily represented in but far from exclusive to the Division of Fluid Dynamic at Chalmers and GKN aerospace Trollhättan.

Finally, I would like to thank my family and friends for your great support and the wonderful individuals you are.

Work in this thesis was financially supported by; VINNOVA in the Swedish National Aviation Engineering Research Programme (NFFP) through project AT3E; Moststrom and AROS; the department of the Department of Applied Mechanics; GKN Aerospace Trollhättan; Chalmers Laboratory of Fluids and Thermal Sciences; and the EU commission in the CleanSky2 programme via project EATEEM and ENABLEH2. This project has received funding from the Clean Sky 2 Joint Undertaking under the European Union's Horizon 2020 research and innovation programme under grant agreement No 821398 and 769241.

Isak Jonsson
Göteborg, Dec 2021

List of Publications

This thesis is based on the following appended papers & proceedings:

Paper A Isak Jonsson, Valery Chernoray, Borja Rojo. *Surface Roughness Impact On Secondary Flow and Losses in a Turbine Exhaust Casing*, Proceedings of ASME Turbo Expo 2018, GT2018-75541.

Paper B Srikanth Deshpande, Isak Jonsson, Valery Chernoray. *Effect of Surface Roughness on Aerodynamic Performance of Turbine Rear Structure*, Proceedings of ASME Turbo Expo 2019, GT2019-90472.

Paper C Isak Jonsson, Valery Chernoray, Radeesh Dhanasegaran. *Infrared Thermography Investigation of Heat Transfer on Outlet Guide Vanes in a Turbine Rear Structure*, Int. J. Turbomach. Propuls. Power 2020, 5(3), 23.

Paper D Isak Jonsson, Srikanth Deshpande, Valery Chernoray, Oskar Thulin, Jonas Larsson *Experimental and Numerical Study of Laminar-Turbulent Transition on a Low-Pressure Turbine Outlet Guide Vane*, ASME. J. Turbomach. October 2021; 143(10): 101011.

Paper E Isak Jonsson, Carlos Xisto, Tomas Grönstedt. *Design of Chalmers new low-pressure compressor test facility for low-speed testing of cryo-engine applications*, ETC2021-554, Proceedings of 14th European Conference on Turbomachinery Fluid dynamics & Thermodynamics, ETC14, April 12-14, 2021, Gdansk, Poland.

Paper F Isak Jonsson, Carlos Xisto, Marcus Lejon, Anders Dahl, Tomas Grönstedt. *Design and Pre-Test Evaluation of a Low-Pressure Compressor Test Facility for Cryogenic Hydrogen Fuel Integration*, ASME Turbo Expo 2021, GT2021-58946.

Other relevant publications by Isak Jonsson:

Paper G Isak Jonsson, Carlos Xisto, Hamidreza Abedi, Tomas Grönstedt, Marcus Lejon. *Feasibility Study of a Radical Vane-Integrated Heat Exchanger for Turbofan Engine Applications*, ASME Turbo Expo 2020, GT2020-15243.

Nomenclature

Abbreviations

ADP	–	At Design Point
CFD	–	Computational Fluid Dynamics
DIT	–	Differential Infrared Thermography
FEM	–	Fenit Element Method
FSD	–	Full Scale Deflection
HEX	–	Heat Exchanger
HPC	–	High-Pressure Compressor
HTC	–	Heat Transfer Coefficient
ICD	–	Intermediate Compressor Duct
IGV	–	Inlet Guide Vane
IR	–	Infrared
LPC	–	Low-Pressure Compressor
LPT	–	Low-Pressure Turbine
MCS	–	Monte Carlo Simulation
MHP	–	Multi-hole Probe
NGV	–	Nozzle Guide Vanes
OGV	–	Outlet Guide Vanes
PIV	–	Particle Imaging Velocimetry
RMA	–	Reflective Marker Array
RPM	–	Rotations per minute
RSS	–	Root Sum Square
SFS	–	Sliding Frame Subtraction
SLA	–	Stereolithography
SST	–	Menter's Shear Stress Transport
TRS	–	Turbine Rear Structure

Latin

A	–	Area
b_1	–	MHP angle coefficient 1
b_2	–	MHP angle coefficient 2
A_t	–	MHP Total Pressure coefficient

A_s – MHP Static Pressure coefficient
C_p – Pressure coefficient
C_{p0} – Total Pressure coefficient
h – Heat Transfer coefficient
K – Acceleration parameter & Kelvin
k_s – Sand-grain
$k_{s,h}$ – Sand-grain roughness height
k_s^+ – Equivalent sand-grain roughness
k – Thermal Conductivity
P^* – Normalised Total Pressure
U – Velocity
R – Reading of value
Re – Reynolds Number
Re_θ – Momentum Thickness Reynolds Number
R_a – Arithmetical mean deviation of surface roughness height
R_q – Root mean square roughness height
R_y – Maximum profile height of surface roughness
Rsk – Skewness of surface roughness height
Tu – Turbulence intensity
T – Temperature
t – Thickness
q – Dynamic pressure
q_c – Quasi dynamic pressure
q'' – Heat flux
P_s – Static pressure
P_t – Total pressure
P_i – Pressure of port or location
P_{amb} – Absolute pressure

Greek

α – Probe angle in XZ-plane & Swirl in the TRS & Thermal expansion coefficient
β – Probe angle in XY-plane
ϕ – Roll angle & Flow coefficient
θ – Cone angle & Load coefficient
δ_v – Viscous sub-layer thickness
δ – Individual error & Momentum thickness
ε – Propagated/total error & Emissivity
ρ – Density
σ – Standard deviation & Stefan-Boltzmann constant

Subscripts

ref – Relative to measurement point
t – Onset of laminar-turbulent transition

Superscripts

$+$ – Port perceiving the highest Pressure
$-$ – Port perceiving the lowest Pressure
$\bar{\xi}$ – Area Average
$\tilde{\xi}$ – Mass flow Average
$\hat{\xi}$ – Time Average

Diacritics

$\bar{\text{o}}$ – Area Average
$\tilde{\text{o}}$ – Mass flow Average
$\hat{\text{o}}$ – Time Average

Contents

Part I

Introductory chapters

Chapter 1

Motivation

Commercial aviation engines are truly marvellous machines. They consist of millions of lightweight parts, rotating at tens of thousands of rotations per minute (RPM) and occasionally operating at gas temperatures above the component melting point. The engines achieve this and still maintain reliable long-term operation, high thermal efficiency and high power density. There is a constant demand to achieve higher power density and reduced component losses from industry and governmental regulations. However, as the fidelity of the individual components approaches the theoretical maximum, there is a diminishing return of performance improvement. Arguably, many aspects of engine performance improvements can be attributed to advances in numerical tools such as Computational Fluid Dynamics (CFD) that have reached such maturity that much of the iterative work conducted experimentally 30 years ago can now be performed using numerical simulations. The increased fidelity of both components and numerical tools has increased the demands on the verification data in all dimensions, spatial and temporal, and the measurement quality itself. Hence, the aerothermal experimentalists' work focuses on exceedingly detailed and comprehensive studies in evermore complex flow fields with high demands on measurement quality to verify component testing and numerical models.

One disadvantage for the experimentalist is that the accuracy of many experimental devices has historically not increased at the same pace as the spatial and temporal resolution. Hence, the experimentalist often cannot simply buy more accurate instruments to achieve higher measurement accuracy instead needs to design the experiments around the instrument accuracy. This issue will be principal throughout this thesis when attempting to improve measurement accuracy for aerothermal studies in internal jet engine structures. Consequently, most of the work presented in this thesis regards uncertainty mitigation and holistic engineering of both facilities and methods to achieve targeted accuracy. Two experimental measurement methods, multi-hole probe (MHP) pneumatic measurements and heat transfer studies utilising Infrared (IR)-thermography, are scrutinised in this thesis.

Multi-hole pneumatic probes are a recognised and established measurement technique in academic and industrial applications and provide flow velocities, angles and pressures at probe tip location. Fundamentally, the technique utilises pressure differences between the ports on a probe to deduce flow quantities. This work

describes the state-of-the-art of the MHP technique and some of the problems when implemented in a low-loss high-dynamic pressure environment.

IR-thermography detects emitted radiation in the IR spectrum. The detected radiation can then, by calibration, be applied to measure surface temperature, among other things. This work focuses on error mitigation when using surface temperature measured by IR-thermography to evaluate surface heat transfer coefficient (HTC) by solving conjugate heat transfer along a vane wall. Further processing of the heat transfer data to detect the laminar-turbulent transition or flow separation is performed and presented in this thesis.

The methods mentioned above have been implemented and developed for measurements in a turbine rear structure (TRS). The experimental results from several projects are merged in this thesis and provide new insights on the aerodynamic and aerothermal performance of an engine representative baseline TRS at a realistic Reynolds number. The influence of surface roughness on aerodynamic performance, heat transfer coefficient distribution, secondary flow structures on the suction side and laminar-turbulent transition location are presented for a baseline TRS.

The methods mentioned have been adapted and developed together with a new low-pressure compressor facility to provide highly accurate aerothermal results for an intermediate compressor duct (ICD). At the time of writing, the low-pressure compressor facility to evaluate the ICD is not yet fully operational, but the facility's design and instrumentation are presented in this thesis and in the appended Papers E and F. This thesis focuses on the measurement techniques and designing the Low-pressure compressor (LPC) facility to achieve the appropriate measurement quality and only touches on the engineering required to get the facilities functional.

Chapter 2

Jet Engine Structures

This section acts as a general introduction to internal jet engine structures regarding their mechanical and aerodynamic usage in commercial jet engines. Many of the generalisations described below are valid for most practical real engine configurations. Internal jet engine structures refer to components that transfer a substantial mechanical load through the core gas path. The ICD and TRS are two such structures located in different sections of the engine and illustrated in Fig. 2.1 using the schematics of a Rolls-Royce Trent-1000 commercial jet engine. The ICD is one of the principal components to transfer the mechanical load from the front bearing through the gas path, while the TRS carries the mechanical load from the rear bearing to the rear engine mount. Geometrically, the two components share some common traits. From Fig. 2.1 one can note the ICD and TRS to have larger and considerably fewer struts/vanes than the adjacent compressor or turbine stages. The struts in these components have a lower aspect ratio and a thicker chord to make them more structurally robust and allow for oil, power and miscellaneous routing to pass through. They accommodate oil hoses for bearing cooling, bleeding of compressed air or shafts for electric power generation. From an aerodynamic point of view, there is a penalty with thicker vanes with the increased wetted surface. Note that all aero surfaces designed by GKN in this work are aimed for the facilities at Chalmers University of Technology and do not represent any GKN product characteristics.

2.1 Aerodynamic Function of the Turbine Rear Structure

The TRS and ICD fulfil different aerodynamic functions in a commercial jet engine. To maximise thrust, the TRS is designed to remove residual swirl at the outlet of the last low-pressure turbine (LPT) stage. The design challenge is to deswirl the flow with minimum losses in the wide operational envelope of the TRS, both in inlet swirl angles and Reynolds number. The Reynolds number in a TRS during engine operation ranges from 100,000 to 600,000. A large part of this wide operational space in Reynolds number can be attributed to the TRS being exposed to ambient conditions as air density change alone causes four-fold Reynolds number changes between take-

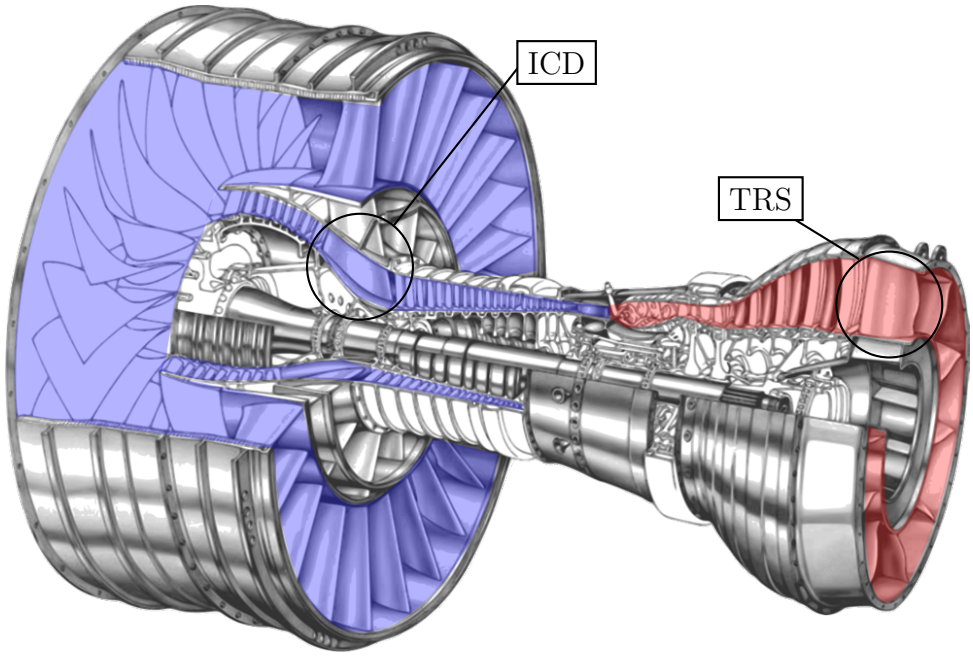

Figure 2.1: Commercial jet engine schematics with colour markup for hot and cold areas, vectorised version from [55].

off and cruise. In addition, changes in engine operation cause changes in temperature, dynamic pressure and swirl to vary, further expanding the operation space of the TRS. One challenge for the designer of a TRS is the specific range of Reynolds number 100,000 to 600,000 where several modes of laminar-turbulent transition can occur. The mode and location of laminar-turbulent transition significantly impacts the turning performance of an airfoil, and a component working adequately at sea level might lose several percentage points in performance at cruise conditions due to this effect alone [33]. With the introduction of the geared and ultra-high bypass engine concept, the operational window for the LPT is further expanded with larger ranges of LPT outlet swirl angles and temperatures. This will further challenge the designer of the TRS.

Figure 2.2a provides an isometric view of the TRS baseline geometry with the upstream LPT stage. Before entering the TRS module, the flow passes from left to right through the nozzle guide vanes (NGV) and the rotating LPT. Seen from downstream, the rotor rotates clockwise while the midspan LPT outlet flow is angled counterclockwise. In Fig. 2.2a, the suction side of the outlet guide vane (OGV) is depicted, where the blue lines show topological streamlines at design condition. The blue shaded area shows the expansion of secondary flow from the leading edge. The green shaded line indicate experimentally observed laminar-turbulent transition locations, and the spanwise arrows show the radial pressure gradient. The two locations of measurement are illustrated in Fig. 2.2a by red and green (red - inlet, green - outlet) planes. Figure 2.2b shows the circumferentially averaged spanwise swirl distribution at the inlet and outlet planes at design point (ADP). The inlet swirl α_{in} has been shifted 16 degrees towards the centre for illustration purposes. At ADP the inlet swirl angle is distributed with a high incidence near the hub and an

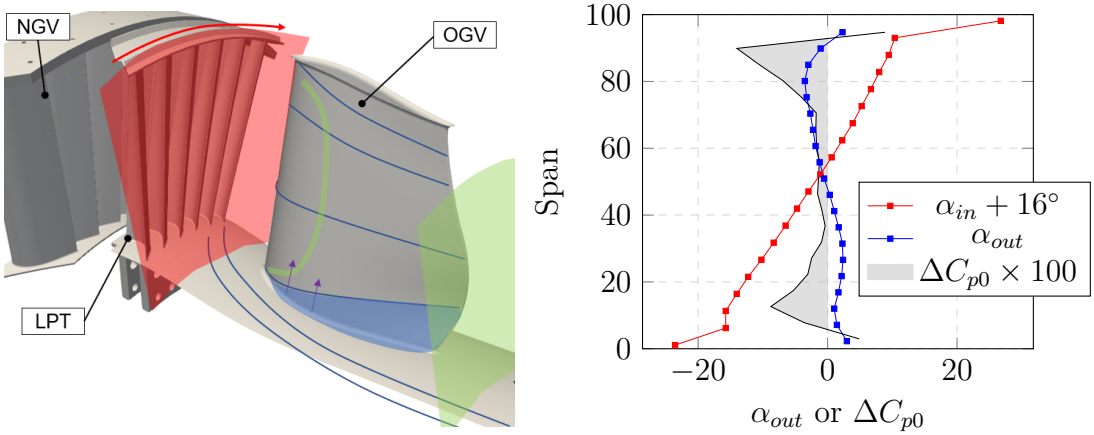

(a) (b)

Figure 2.2: To the left is the topology of the TRS from experimental studies, with streamlines in solid blue lines, transition location in green lines, and inlet and outlet in red and green planes, respectively. To the right is typical circumferentially averaged inlet and outlet flow angles at the design point in the TRS together with the normalised loss distribution.

adverse incidence near the span. For an OGV of good aerodynamic design the outlet swirl angle is close to zero. The spanwise loss distribution at ADP is shown as a grey shaded area with low losses at midspan and substantial values near the outer and inner casing. To achieve an axial outlet flow, the hub region of the OGV is forced to perform substantially more deswirling than the rest of the vane. This blade loading is typical for stators both in turbines and compressors, and the same topological terminology can be used for the secondary flow structures concisely summarised by Harvey [21]. At design conditions, the high blade loading near the hub causes favourable conditions for the growth of the low momentum secondary stream tubes, near-wall separations and cross-flow structures. These secondary flow structures comprise a large part of the component overall losses and is reflected in the spanwise averaged loss distribution shown in Fig. 2.2b, with significant losses at 0–25% span. At 80–100% span, the local pressure loss is partly caused by mixing the LPT tip leakage flow and partly due to secondary flow losses. In general, the secondary flow losses are reduced with blade loading, and at extreme off-design conditions, profile losses become dominant. For most operational conditions, the losses are located in a near-hub region in the suction side region, and this thesis focuses on measurements in this region and the likely sources of these losses.

TRS operates in the hot core gas path, and thermal loads caused by the hot gas directly affect the mechanical integrity of the TRS. Thus, one key challenge is to predict the convective heat transfer between the gas and the walls, which is experimentally addressed in this work in Chapter 3 and Paper C.

Several previous studies of the TRS have been performed in a linear cascade where the significant three-dimensional effect cannot be replicated. Hjärne et al. published several aerodynamic studies of a midspan OGV in Chalmers linear cascade [22, 23, 24]. In the same facility, Rojo et al. [43] and Wang et al. [56] performed heat transfer studies. Both numerical and experimental aeroacoustic studies have

been performed at TU Graz using an annular TRS with Reynolds numbers up to 120,000 in [32, 50]. Prior the studies in the Chalmers' LPT-OGV facility, there were no such experimental studies in the public domain known to the author for a TRS at Reynolds numbers higher than 120,000.

The aerodynamic design of the TRS and surrounding components fall outside the scope of this work, and GKN Aerospace Sweden performed the aerodynamic design of all turbomachinery parts of the LPT-OGV facility.

2.2 Aerodynamic Function of the Intermediate Compressor Duct

In the ICD, the challenge is to efficiently guide the flow from the LPC to the high-pressure compressor (HPC) via an S-shaped duct with a minimal axial distance, i.e., as short as possible at a minimal pressure loss. Since the flow exiting the ICD enters the HPC, the outlet of the ICD must be compatible with the HPC. An isometric view of the studied ICD is provided in Fig. 2.3 with the core flow entering from the left. The outlet flow from the upstream LPC is deswirled by the LPC-OGV so entering the ICD is nearly axial. In the duct, struts transport the mechanical loads between the outer and inner casings and is located in the gas path.

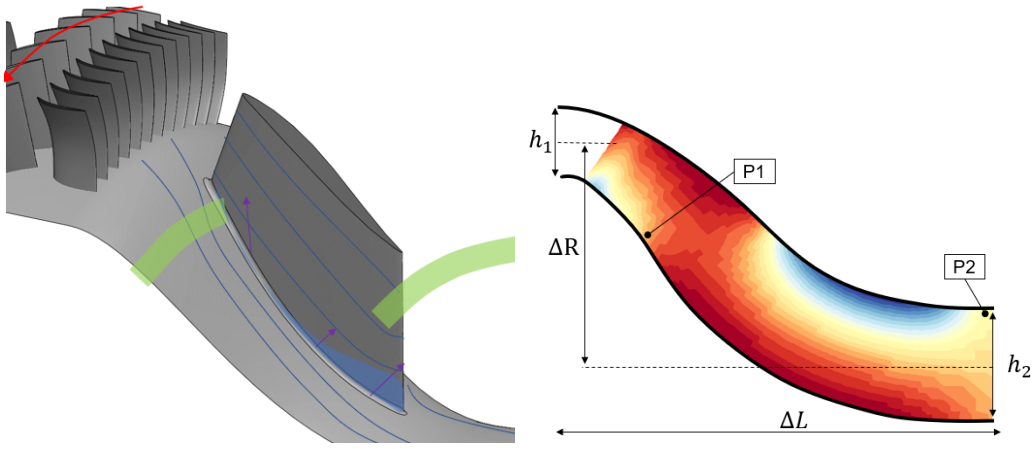

(a) (b)

Figure 2.3: (a) Flow topology in an ICD follow the same markings as in Fig.2.2a and (b) C_p distribution including fundamental design parameters for the ICD.

Keeping the radial distance ΔR constant as the duct's length ΔL is reduced (see notations in Figure 2.3a), the fundamentally limiting factor is the adverse pressure gradient that arises on the concave parts of the S-duct. Two locations with an adverse pressure gradient are marked out in Fig. 2.3b, one at the hub (P1) as the core flow is guided radially, and one at the shroud when the flow is guided axially (P2). The adverse pressure gradient at the second point can be reduced by accelerating the flow in the downstream part of the duct, e.g, by reducing the cross-section area ratio A_{in}/A_{out}. The abovementioned parameters are standard design parameters of

an ICD.There are several several additional factors that impact the performance of the ICD. The flow entering the ICD is not uniform, with static and rotating wakes from the upstream compressor and LPC-OGVs. Britchford et al. [7] showed the importance of a non-uniform ICD inlet where high turbulence near the endwalls would energise the boundary layer, which with all else equal, would allow for a 21% shorter duct. Second, the duct is is not smooth as bleed valves are commonly placed somewhere along the shroud line, disturbing the flow. Chen et al. [10] showed that by ejecting the boundary layer at the shroud, the low momentum boundary layer is removed, and the losses in the duct can be reduced. Walker et al. [53] showed increased stability of the duct by ejecting the boundary layer from the duct at the hub. Bailes et al. [4] experimentally investigated and demonstrated the effects of struts on local acceleration and the negative impact these accelerations has on the pressure losses in the duct. Siggeirsson et al. [49] showed that the upstream secondary flow structure from the OGV hub area can interact with the secondary flow structures from the struts with significant effects on the uniformity of the outlet flow.

Hence, in a real ICD the adverse pressure gradient is the key limiter, although with strong influence from the complex flow structures. The topological flow structures in the ICD are shown in Fig. 2.3a, where the blue lines represent streamlines at design conditions. The blue shaded area indicates the expansion of secondary stream tubes from the leading edge stagnation point. The green shaded areas show where adverse pressure gradients are expected to impact the laminar-turbulent transition and separation of the boundary layer significantly. A horseshoe vortex occurs at the leading edge of the strut, both at the shroud and hub. Because the flow is decelerated near the hub, the hub vortex expansion is substantially larger than at the shroud. As demonstrated by Siggeirsson et al. [49], this area is also sensitive to wake integration with upstream flow features such as OGV wakes.

2.3 Fundamental Similarities

Even though the two components' aerodynamic purpose and design challenges are significantly different, they share many similarities and flow phenomena, listed below.

- Both components have critical areas where several modes of laminar-turbulent transition and separation might occur over an engine operation space. As shown in Fig. 2.3a, the sensitive locations for the ICD are at the hub and shroud lines. For the TRS, illustrated in Fig. 2.2a, the critical area is on the suction side, especially near the hub.

- The thicker struts/vanes in the ICD and TRS are of low aspect ratio and located relatively far downstream of a stage with a much higher blade count and blade aspect ratio. This causes wake and secondary flows interaction that is very different from typical rotor-stator interaction where aspect ratio, blade height and number are similar.

- The low aspect ratio together with the strong radial pressure gradient has a significant impact on the secondary flow, which in both cases is the primary source of pressure losses in a large portion of the operational space.
- There are no shocks present in either of the components, making incompressible studies feasible for both.
- The upstream units (LPC and LPT) cause complex three-dimensional inlet conditions with mixed end-wall boundary layer, stator and rotor wakes, high swirl variations and pressure gradients that significantly affect the aerothermal performance of the investigated unit.
- The high complexity and relatively high fluctuations in the flow inside both the TRS and ICD make normalisation and differential measurements challenging.
- The thick and non rotating vanes enable easy implementation of pressure taps and highly accurate heat transfer measurements.

2.4 Hydrogen Fuel Integration

Hydrogen has in recent years gained considerable traction for de-carbonisation of both industrial processes and the general energy mix. In the aviation industry, liquid hydrogen (LH_2) is a prime candidate due to the high specific heat capacity at cryogenic temperatures. The cryogenic storage requires adequate insulation and the integration of heat exchangers (HEX) to heat the fuel before injecting it into the combustion chamber. For example, injecting the hydrogen in the combustor at 25K instead of 1000K, 10% of the lower heating value would be lost to heat the fuel, i.e., potentially a 10% penalty in thermal efficiency (with all else equal and a lossless system). The energy required to bring the cryogenic hydrogen to a suitable combustion temperature is substantial but a valuable heat sink for several processes. Part of the work at Chalmers in the ENABLEH2 project is to design and test systems to preheat the fuel by the core flow. The cold temperature and high specific heat capacity of the fuel allow for compact HEX that can synergistically be integrated into existing components. Two prime candidate for this HEX integration is the ICD and TRS, both due to the strategic location in the engine and function. The TRS can be utilised to recover some of the heat rejected in the exhaust, and the ICD can be utilised to pre-cool the core flow before entering the HPC. The existing wetted surface in TRS and ICD is not likely to be sufficient for the cooling power required, so an increased surface area for any HEX integration is likely. The increased surface area comes with a penalty in increased friction losses, but the same surface can also increase the components' turning abilities by unloading existing surfaces. In the TRS, the increased surface can aid in de-swirling the LPT outlet and offload the OGV, making it more robust for off-design conditions. In the ICD, the increased surface could assist radially in guiding the flow and make the duct shorter with a more uniform outlet. A concept of TRS with splitter vanes is shown in Fig. 2.4a.

A feasibility study of the integration of one potential implementation in the ICD is presented in Paper G and shown in Fig. 2.4b

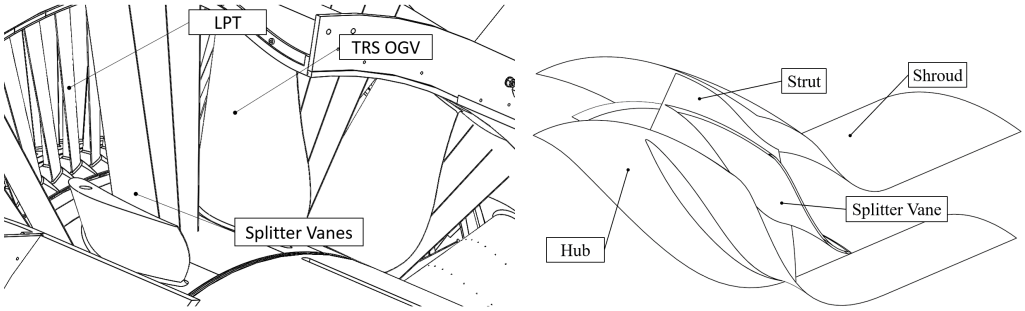

Figure 2.4: Implementation of splitter vanes for increased wetted surface and turning ability in the TRS (left) and ICD (right).

The design challenges of these two integrated heat exchangers are similar, and from an experimental point of view, near-identical, further expanding the overlap in the similarities between the ICD and TRS.

2.5 Facility Overarching Approaches

As described earlier, the two facilities in this work share a lot of instrumentation and many challenges. The development of specific methods was mainly conducted in relation to the work at one or other of the facilities. The method development and discussion of each method are therefore split between the facilities, according to the facility at which the work was carried out. This section discusses some overarching challenges and clarifications regarding data normalisation.

2.5.1 Error Mitigation

As already mentioned, error mitigations in this work are based on uncertainty analysis and comparison between configurations. An uncertainty analysis provides a clear prioritisation by revealing the size of the contribution of independent variables x_i and whenever the measurements are feasible for the target level of accuracy. The engineering specifics of error mitigation (either by new manufacturing methods, measurement methods or a change in approach) are individual to each problem. However, the tools used to conduct an uncertainty analysis are general and thus described in this section.

To better understand the basic principle, the phrase "error mitigation" might better be described as "error balancing" or "error optimisation". Consider the generally agreed engineering approach of approximating the combined independent error sources ε_i using the root sum squares (RSS) as in Eq. (2.1). It may then be observed that a slightly more significant contributor of one of the sources becomes dominant. With independent variables, the apparent mitigation is in minimising peak values of ε_i. However, since the researchers often use the most accurate devices available, this is rarely an option. Hence, it is necessary to re-engineer the experimental set-up

and optimise it to minimise the overall error ε_{tot}. This is occasionally achieved by changing the operational conditions, positioning sensors to mitigate bias offset and reducing traducers measurement ranges, but an entirely new approach is often required. The optimal result in this case is the lowest summed error that is practically possible, with emphasis on practically.

$$\varepsilon_{tot} = \sqrt{1/n \sum_{1}^{n} \varepsilon_i^2} \tag{2.1}$$

The process is relatively straightforward with independent errors, but in near all applications, errors are not independent and not equally weighted. Methods such as Taylor Expansions and Monte Carlo Simulation (MCS) provide an assessment of the uncertainty contribution from each individual error source x_i to the final uncertainty ε_ς for an expression or a system.

The Taylor expansion method relies on Eq. (2.2). To the best of the author's knowledge, this method was first formulated by Ku [29] but is commonly used in standards such as ASME PTC 19.1 [2] or ISO 17025 [25]. The Taylor expansion can be used where the expression can be formulated analytically, the data assumed to be normally distributed and linear error predictions are reasonable. The dependable function is ς, x_i are the independent variables of the expression and the error of each independent variable is represented by δ_{x_i}.

$$\varepsilon_\varsigma(x_1, x_2, ..., x_n) = \left\{ \sum_{i=1}^{n} \left(\frac{\partial \varsigma}{\partial x_i} \cdot \delta_{x_i} \right)^2 \right\}^{1/2} \tag{2.2}$$

Equation (2.3) describes the implementation for uncertainty propagation estimation by the use of the MCS method. The MCS method [44] is empirical and can be utilised on black-box systems but do not, in general, provide the clear cause of errors and ways to reduce them as the Taylor series does. The MCS method can be generalised for most error estimations by Eq. (2.3). Perturbations δ are introduced on the average value x_i and introduced error on the function ς can be estimated as ε_ς. By introducing a significantly large population of perturbations and using statistical assumptions, the uncertainty of the function ς can be estimated.

$$\varepsilon_\varsigma = \varsigma(x_1, x_2, ...) - \varsigma(\widetilde{x_1}, \widetilde{x_2}, ...) \quad \widetilde{x_i} = x_i + \delta_i \tag{2.3}$$

Any valid statistical input can be utilised for the perturbations. If not otherwise specified in this work, the input perturbations are assumed to be Gaussian distributed. All analytical and empirical investigations were performed using in-house Matlab™ scripts. For example, the entire analytical expansion of the heat transfer error estimation was more than 26,000 characters long and would not have been feasible to perform without the symbolic package in Matlab™.

2.5.2 Data Normalisation/Reductions

This section summarises the challenges and motivations of data normalisation utilised in the TRS, LPC and ICD.

Experiments in fluid dynamics are, in general, unsteady by nature. In the TRS, LPC and ICD, several parameters fluctuate from day to day or moment to moment. Room pressure, room temperature, water temperature, the operational point of the fan, the operational point of upstream turbomachinery and humidity are all examples of properties that change during and in between each experiment. The fluctuation can be in the same order of magnitude as the sought quantity x_i. Data normalisation aims to make data that has been sampled at different times and locations, and therefore under different conditions, equivalent. The most apparent method to normalise the measured data is trhough multipliers of the mean properties in the flow. The challenge is often to find this multiplier.

Data presented in Papers A,B and D have utilised a static probe to represent both time x_i and average fluctuation $\bar{x}_i$. A single reference probe is well suited to capture minor time-dependent fluctuations for the duration of the experiment. However, with any significant redistribution of the flow, for example, at a new operational point, there is no guarantee that the under-sampled reference (a single location in this case) will perceive the mean changes of the flow. If the reference probe fails to capture the mean value change accurately, it will cause an offset in the normalised quantity. Nevertheless, the single probe has worked satisfactorily to compare cases as the reference probe value has been located in a low gradient area and sometimes adjusted between extreme operational conditions to represent the average flow changes better.

The normalisation in Paper E might be the simplest to start with as it uses the normalised total pressure P^* as defined in Eq. (2.4). The measured pressure in a given spatial point $P_{t,i}$ is normalised by the pressure found at the reference $P_{t,ref}$ measured in the same time frame. This normalised value is multiplied with the averaged reference probe pressure $\bar{P}_{t,ref}$ for the entire dataset. Note that for P^*, C_{p0} and C_p, index i represents a position and not variables.

$$P^* = P_{t,i}\frac{\bar{P}_{t,ref}}{P_{t,ref}} \tag{2.4}$$

The P^* was derived as an alternative to normalisations used in [42], Paper A and Paper B where the reference pressure was subtracted from the referenced probed value $P_{t,ref}$ and divided by the dynamic pressure, q_{ref}.

$$Cp_0 = \frac{P_{t,i} - P_{t,ref}}{q_{ref}} \tag{2.5}$$

$$Cp = \frac{P_i - P_{ref}}{q_{ref}} \tag{2.6}$$

The three different normalisations have been shown to perform satisfactorily to normalise pressure fluctuations in the TRS. Following the formulation of P^*, a general normalisation can be written as in Eq.(2.7). The reference probe perceived value is shown as x_{ref} and the sample average as $\bar{x}_{ref}$. The probed value is x_i at location i and x_i^* is the normalised value.

$$x_i^* = x_i\frac{\bar{x}_{i,ref}}{x_{i,ref}} \qquad x_i = p_0, T, ... \tag{2.7}$$

The challenges in the LPC are different from the TRS and ICD as the normalised values are used to calculate the performance in absolute values. Therefore, the scaling reference needs to be selected with care so that any bias offset in the reference has a limited effect on the evaluated performance.

As mentioned, a single probe as used in the TRS is not guaranteed to capture the actual average changes of the flow. Methods such as rakes, several probes or pressure taps along the end-walls are common solutions to increase the reference value's likelihood to capture the actual mean flow changes. All these methods are, to a substantial degree, under-sampling the flow field. If this under-sampling is acceptable is case dependent.

A relatively time-consuming solution to this problem is proposed in Paper F. First, a single static reference probe captures the relatively small time-dependent fluctuations. To cope with the under-sampling of a single probe, the reference probe dataset average $\bar{x}_{i,ref}$ in Eq.(2.7) is scaled against a better representation of the actual flow average $\bar{X}_i$. Paper F utilises the mass-flow weighted average of a traversed area for scaling the single reference. The scaling is represented as coefficient c_x in Eq. (2.8) where $\bar{x}_{i,ref}$ represents the reference probe perceived flow properties during the traversing. Traversing is a relatively time-consuming process, but a sufficient number of points provides an estimation of the area average value $\hat{x_{i,trav}}$.

$$c_{x_i} = \frac{\overline{X_i}}{\overline{x_{i,ref}}} \approx \frac{\hat{x}_{i,trav}}{\overline{x_{i,ref}}} \qquad x = p_0, T, ... \tag{2.8}$$

There are several variations of the implementation of Eq. (2.8), one is to use the area average c_x to scale an absolute value of the $\overline{x_{i,ref}}$. Another implementation is to utilise the scaling on each spacial location before averaging. When using the average, c_x is a scalar, and the implementation can be described by Eq.(2.9).

$$x_i^* = x_i \frac{\bar{x}_{i,ref}}{x_{i,ref}} c_x \qquad x = p_0, T, ... \tag{2.9}$$

The time-consuming aspect is that the area needs to be re-traversed if any substantial flow redistribution occurs. However, from experience in the TRS, this will not be a large drawback as the inlet and outlet boundaries are traversed for nearly all cases.

The location of the reference probe should be located to capture relevant fluctuations in the flow field. Often the inlet is selected for the reference probe due low pressure and velocity gradients in the flow. A high gradient area downstream the last rotor is selected for the reference for LPC performance evaluation as it includes fluctuations related to the compressor performance. The same location is also suitable for ICD investigations, further motivating this high gradient location.

Chapter 3

LPT-OGV Test Facility

3.1 General Description

This section provides the general characteristics and capabilities of the Chalmers LPT-OGV test facility, which was built to evaluate the aero-thermal performance of the TRS module experimentally. The general description in Section 2 provides a sufficient background to discuss challenges and instrumentation in the TRS, but more details about the facility can be found in [42].

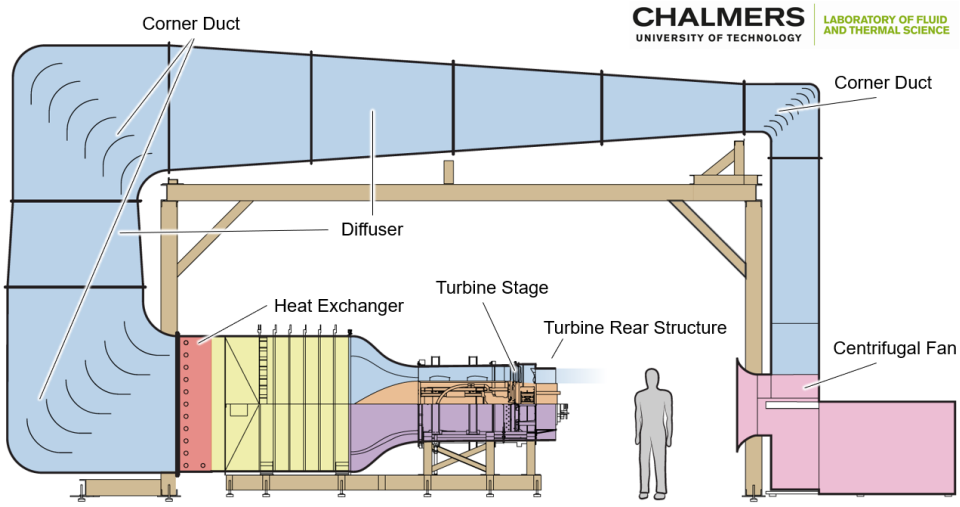

Figure 3.1: Chalmers LPT-OGV facility.

The Chalmers LPT-OGV test facility is an annular semi-closed 1.5 LPT stage test facility built to test the aerothermal performance of the TRS in various engine-representative flow conditions. Figure 3.1 shows the schematics of the facility together with a manikin for scale. A centrifugal fan drives the facility. Downstream of the fan, the main flow is diffused and guided through several corner ducts and through a 2 m $\times$ 2 m shim heat exchanger. The heat exchanger is used to regulate the main flow temperature using water from the central cooling system. Downstream of the heat exchanger, the main flow passes through a flow conditioner of stainless steel screens, and an aluminium honeycomb, which was designed following guidelines from

[5, 6, 20]. Before entering the turbine section, the main flow is accelerated through the contraction optimised by Rojo in [42]. The aerodynamic design of the LPT stage was performed at GKN Aerospace Trollhättan Sweden, and it was mechanically designed at Chalmers. A hydraulic brake regulates the turbine rotational speed in the TRS stage. Downstream of the single LPT stage, the main flow goes through the TRS module, the outlet of which is directed towards the inlet of the centrifugal fan to recover the residual dynamic pressure.

The operational envelope of the facility in terms of Reynolds number and midspan inlet swirl variation is illustrated in Fig. 3.2. The figure further includes examples of aircraft engines in relation to their operational Reynolds number. As the Reynolds number increases, the range of possible inlet swirl is limited by the LPT operation. The targeted design conditions at a Reynolds number of 465,000 for the facility is shown as a red marker in Fig. 3.2. Tests in the facility have been performed at Reynolds numbers as low as 50,000 up to design conditions at 465,000. Tests at higher Reynolds numbers can be performed with limited modifications on the flow conditioner and allow the facility to create representative flows of conditions found in engines as large as the GP7000.

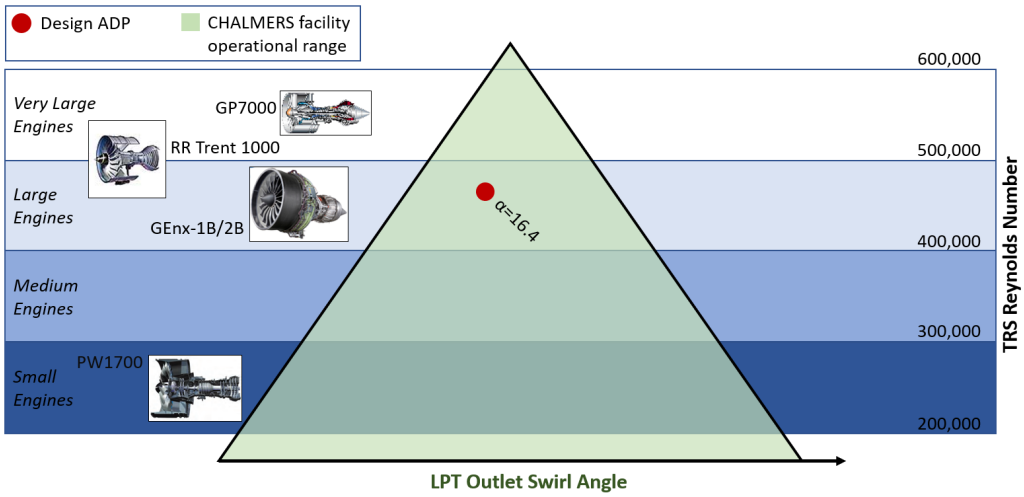

Figure 3.2: Chalmers LPT-OGV test facility operational space.

3.2 TRS Module

The TRS module is constructed to be modified so each aero surface such as the OGV, shroud, P-flange pocket, purge-flow and hub can independently be exchanged or instrumented. Figure 3.3 shows an isometric view of the TRS, including three types of instrumented OGVs. Marked as B is the heated vane used for heat transfer (described in Sec. 3.3.2). A vane installed for flow visualisation (marked with A) is down to the left, and the one to the right is instrumented with pressure taps (marked with C). The instrumented OGVs are made by Stereolithography (SLA), and two detailed views of the internal water and pressure channels are shown in Fig. 3.2. Two probe traverse systems are installed in the TRS, one upstream (marked with

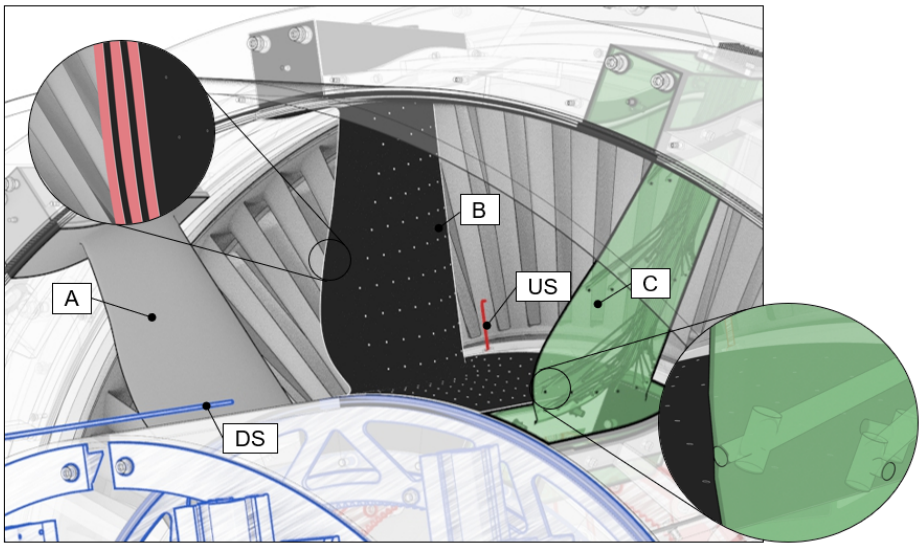

Figure 3.3: Isometric view of the test section with instrumentation location of the MHP and instrumented OGVs for heat transfer and pressure taps. See text for further details.

US) and one downstream of the OGVs (marked with DS). Both systems cover a full 360-degree and full radial range of the channel. In addition, the downstream traverse system is capable of axial motion to access intermediate planes downstream and between each OGV. The two traverse systems together enable a near full-volume 360-degree access of the TRS. In the test section, there is a static Prantl tube for measuring total and static pressure for data normalising as described in section 2.5.2.

Baseline instrumentation is two multi-hole probes, one mounted on each traverse system and pressure taps installed on one or several OGVs. As the TRS module is modified often and substantially, the instrumentation varies. At the time of writing, instrumentation such as hotwire, particle imaging velocimetry (PIV), oil flow visualisation and IR-Thermography has been successfully implemented. The pressures of the multi-hole probe and pressure taps are measured using a Pressure Systems PSI-9116 with a calibrated range of $\pm$ 2500 Pa.

3.3 Instrumentation Development

This chapter presents the implementation and development of the multi-hole probe measurement technique and IR-thermography used in the appended papers. The fundamentals of each method will be introduced, followed by the main challenges and how these were mitigated. Finally, data related to experiments in the TRS are presented.

3.3.1 Multi-hole Probe

As the name suggests, the multi-hole probe is a probe with multiple holes at the tip. The shape of the tip or the number of holes varies depending on the type of probe,

with the most common being five or seven holes with a conical or semispherical tip. The basic operation of a multi-hole probe is simple. As the probe is angled in the flowfield, the surface on the windward side will perceive an increased component of the stagnation pressure, while the surface on the leeward side will perceive a reduced static pressure. The pressures observed at the ports provide the flow angle, the total and the dynamic pressure in the flow.

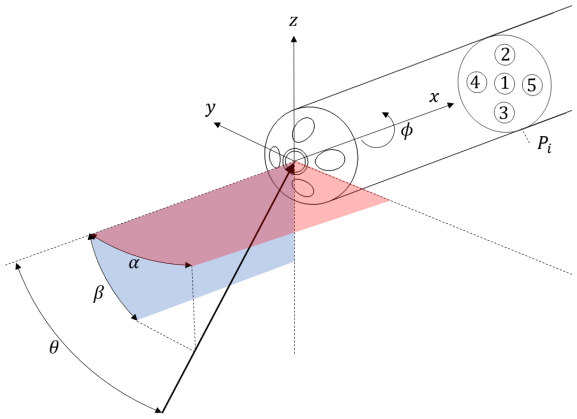

Figure 3.4: Probe coordinate systems and port indexing P_i for a five-hole probe.

A typical five-hole probe is shown in Fig. 3.4 with port numbering and two associated coordinate systems. The coordinate systems are based on the angle between the probe tip and the direction of the flow. The (α - β) coordinate system is based on angle components in the $x-y$ and the $x-z$ planes in Cartesian coordinates. The flow is parallel to the probe when both α and β are zero. The second coordinate system ($\phi-\theta$) is based on a sphero-conical coordinate system relative to the x-axis. At flow parallel to the probe, the roll angle ϕ becomes undefined while the cone angle θ is zero. A multi-hole probe can be used in flow angles up to the point when substantial separation occurs on the leeward side of the probe. For a typical five-hole probe, this occurs at a cone angle of $45-60°$.

A MHP can either be used in a nulling mode or a non-nulling mode. The non-nulling mode is also known as the calibrated mode. The nulling mode is based on finding a set ratio between the ports by orienting the probe in the flow. The nulling mode can be suitable for two-dimensional flow, but the probe's orientation can be problematic for highly three-dimensional flow or narrow spaces. The nulling mode can be made extremely sensitive to small flow angles by connecting opposite side ports differentially.

The second mode is the non-nulling mode, where the probe is calibrated before measurement. This is achieved by traversing the probe in a known flow field for a comprehensive set of flow angles. The pressures from the probe ports are reduced to dimensionless pressure coefficients and correlated with calibration flow pressures and incidence angles. These dimensionless coefficients are later used when the probe is inserted into an unknown flow field. The non-nulling method is the most common implementation.

There are several formulations of dimensionless pressure coefficients. The most commonly used is the sectoring approach, as utilised by Barker et al. [17] and Crawford et al. [12]. In this formulation, there are two definitions of the coefficients depending on the relative flow angle. Equation (3.1) is used when the centre port senses the highest pressure i.e., flow at small cone angles. The second formulation, Eq. (3.2), shows the same coefficients when one of the side ports senses the highest pressure, i.e., when the cone angles are large. This formulation is used in the Chalmers Laboratory of Fluids and Thermal Science and all attached papers.

$$angles \begin{cases} b_1 = \dfrac{P_2 + P_4 - P_5 - P_3}{2q_c} \\ b_2 = \dfrac{P_5 + P_2 - P_3 - P_4}{2q_c} \end{cases}, Pressure \begin{cases} A_t = \dfrac{P_1 - P_t}{q_c} \\ A_s = \dfrac{q_c}{P_t - P_s} \\ q_c = P_1 - \sum_{i=2}^{5} \dfrac{P_i}{4} \end{cases} \tag{3.1}$$

Subscript i is used for the port with the highest measured pressure. The adjacent side ports are denoted by superscripts $+$ and $-$ for high- and low-pressure pressure sides, i.e., windward and leeward, respectively.

$$angles \begin{cases} b_1 = \dfrac{P_i - P_1}{q_c} \\ b_2 = \dfrac{P_i^+ - P_i^-}{q_c} \end{cases}, Pressure \begin{cases} A_t = \dfrac{P_1 - P_t}{q_c} \\ A_s = \dfrac{q_c}{P_t - P_s} \\ q_c = p_i - \dfrac{P_i^+ - P_i^-}{2} \end{cases} \tag{3.2}$$

The q_c is the quasi dynamic pressure, which is proportional to the real dynamic pressure. The variables b_1, b_2 and q_c from Eqs. (3.1) and (3.2) are used to formulate a flow angle interpolation function f as defined in Eq. (3.3) using values from the calibration apparatus.

$$\xi = f(b_1, b_2) \qquad \xi = \alpha, \beta, \phi, \theta, A_{tot}, A_s \tag{3.3}$$

When employed in an unknown flow field, Eqs. (3.4) and (3.5) are used to calculate the pressures. The angles α, β, ϕ and θ are obtained from the interpolation function f.

$$P_{tot} = p_i A_{tot}(b_1, b_2) q_c \tag{3.4}$$

$$P_s = P_{tot} - \frac{q_c}{A_s(b_1, b_2)} \tag{3.5}$$

The calibration is valid as long as the flow field during the calibration represents the unknown flow field in terms of Ma number, Reynolds number, flow angles together and an intact probe geometry.

A flowchart representation of a MHP usage, from calibration to final values, is shown in Fig. 3.5. Dashed lines and boxes indicate that new errors are introduced

to the process. Most boxes and arrows have a general clarification of the processes or the data being transmitted. During calibration, the ambient flow properties are gathered together with probe port pressures, and measurement errors are unavoidably introduced in this process. The port pressures and flow properties are converted into dimensionless values using Eqs. (3.1) and (3.2) and used to formulate the interpolation function f. Further measurement errors are introduced during measurement, which propagate into the dimensionless coefficients b_1 and b_2. By chosen interpolation algorithm, b_1 and b_2 are utilised in function f to extract the flow angles α and β and total and static pressure coefficients. This interpolation of f is imperfect and introduces interpolation noise into the process. To access pressure readings from the MHP, the dimensionless total and static pressure coefficients provided from f require a scaling reference. The scaling is performed using the quasi dynamic pressure q_c as shown in Eqs. (3.4) and (3.5). The calibration, data reduction and interpolation for a five-hole used in the TRS module are described in detail in the next section.

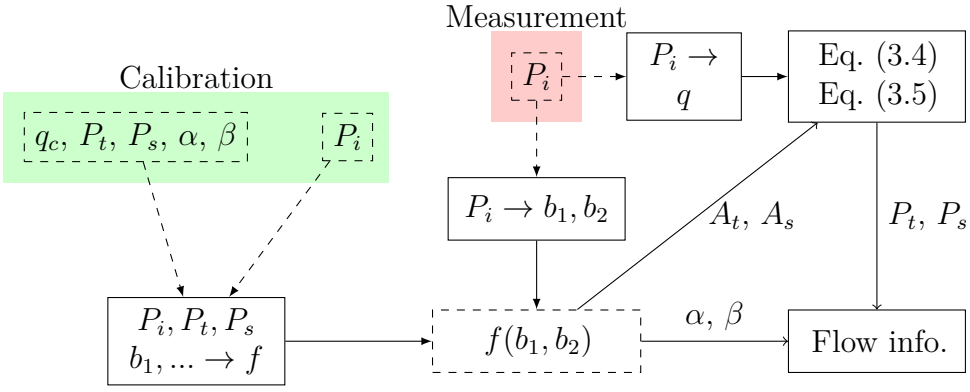

Figure 3.5: Flowchart of the MHP calibration and measurement process

Calibration

At the Chalmers Laboratory of Fluid and Thermal Sciences, the calibration is performed in a jet facility. A centrifugal fan powers the flow, and a flow conditioner straightens the flow before entering the nozzle. Figure 3.6 shows the calibrator schematic with the flow entering from the left. The calibrator nozzle has a contraction area ratio of four, and the differential pressure over the contraction is monitored by a highly accurate micromanometer (FCO560), which provides the dynamic pressure in the jet. The pressure range of the FCO560 is 2000 Pa with an accuracy of 0.1% of the reading (0.1%R) with a $1.5e^{-5}$ full scale deflection (FSD) or 0.03 Pa. Errors are summed using Root Sum of Squares (RSS), but, as shown later, it is occasionally beneficial to keep the statistical and random and bias error separated. A Prantl or Kiel probe is added in the jet several probe diameters far from the probe to capture the total or static pressure variation during the calibration. The temperature is measured with a PT-100 probe, with an uncertainty of ($0.02R \pm 0.1$ K). The reference probe and port pressures are measured with a digital multichannel pressure system PSI-9116 with $\pm$ 2500 Pa pressure sensors mounted. The manufacturer specifies the

accuracy of the PSI-9116 as being 0.15% FSD. However, during internal calibrating against the FCO560, the uncertainty for the unit is better approximated by (0.15%R, 0.15%FSD) or equivalent (0.15%Rpm0.5 Pa).

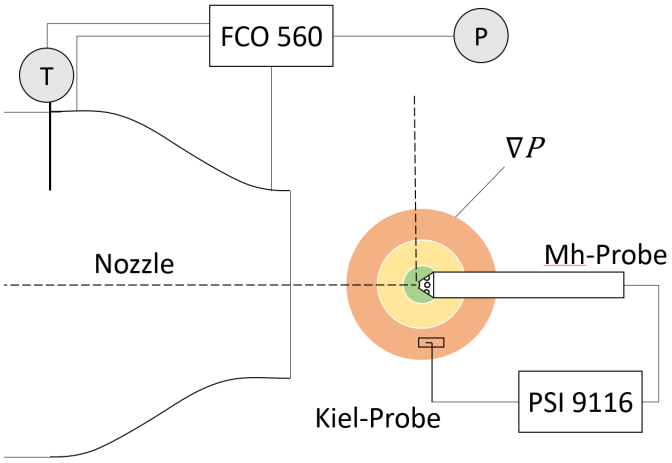

Figure 3.6: Schematics of the probe calibrator in the laboratory.

Centred around the probe in Fig. 3.6 is a schematic static pressure field illustrated by contours. A low-speed jet is often assumed to have the static pressure as the ambient pressure, but the measured pressure gradient 30mm downstream of the nozzle was approximately 0.2% of the dynamic pressure per mm. This relative minuscule gradient is sufficient to affect the calibration accuracy since any misposition or misalignment can offset the total pressure. Two motors with encoders perform the traversing of the probe, and the probe is manually aligned and oriented parallel in the nozzle flow. The position accuracy of the traverse system is significantly higher than the sensitivity of the probe, so errors from encoders and angle alignment from motor encoders are neglected. Many bias errors introduced in the calibration process can largely be ignored when measurements are performed with probes from the same calibrator and calibration procedure, and the relative difference between the two probes are sought. Constant bias errors, such as the geometrical uncertainties of the nozzle, propagate through the calibration and measurement process and essentially cancel out when the measurements between the two probes are subtracted. Therefore, the uncertainties in the calibration process can be divided into two groups, one where the probe is used alone, and absolute values are sought, and one where the relative difference between two probes are used. A summary of the uncertainty for the equipment is shown in Table 3.1. In Table 3.1, the first row shows uncertainty in the calibration process errors of the calibration when measuring relative change between two probes. When using a single probe, the second row should be considered. The values shown in Table 3.1 represent the values introduced in the green box in Fig. 3.5.

Uncertainty from Data Reduction and Interpolation

When analysing the uncertainty of the MHP, the propagation of errors throughout all evaluation chains is required. Since the formulation of dimensionless MHP coefficients

Table 3.1: Individual random and bias errors during the calibration at a dynamic pressure of 900 Pa

	q	P_s	P_t	$\alpha + \beta$ [Deg]	P_i [Pa]	T [K]	P_{amb}
Cal	0.1R	0.4 Pa	0.1R + 0.4 Pa	0.03	0.15R + 0.5 Pa	0.02	0.015
Abs	0.13R	0.9 Pa	0.15R+ 0.9 Pa	0.03	0.15R + 0.5 Pa	0.1	0.2

is analytical, both Taylor expansions and the MSC method can be applied to assess the uncertainty. Utilisation of Eqs. (2.2), (3.1) and (3.2) provides the expected uncertainty. The Taylor expansion provides individual contributions from each independent variable to each dimensionless coefficients A_t, A_s, b_1, b_2 and q_c. To asses the uncertainty of formulating the dimensionless coefficient using the MCS method, Eqs. (2.3), (3.1) and (3.2) are combined using the same assumption for individual errors as with the Taylor expansions. In Table 3.2, the uncertainty of the dimensionless coefficient is shown when using Taylor expansion on Eqs. (3.1) and (3.2).

Table 3.2: RMS of individual uncertainty at a dynamic pressure 900 Pa in the jet

	b_1	b_2	A_t	A_s	α	β	q
Cal	0.2%	0.19%	0.28%	0.1%	0.075	0.075	0.10
Abs	0.2%	0.19%	0.48%	0.3%	0.075	0.075	0.15

The interpolation function used in the thesis is a local linear interpolation scheme. The calibration is divided into local sectors based on the maximum port pressure. The sectoring is illustrated in Fig. 3.7a in relation to flow angles, with the port number perceiving the highest pressure written on the colour-coded sectors. Data from the neighbouring interpolations sectors are used when interpolation is performed along the boundaries of the sectors. A non-symmetric sector distribution would indicate aerodynamic imperfections, although this is not observed in Fig. 3.7a. Figure 3.7b shows the total pressure coefficient A_t for the sector when the centre port is perceiving the highest pressure. The parabolic shape of the coefficient relative to b_1 and b_2 is used in later discussions.

To evaluate the MHP method, two calibration datasets, baseline and post-hoc were created in the same calibrator directly after one another. The two calibrations are identical but with a shift of the calibration grid in terms of α and β. Each calibration dataset consists of 2800 data points and was conducted at speeds and flow angles representative of flow in the TRS. If not otherwise specified, an uncertainty evaluation performed on the baseline data set yielded exactly the same or very similar results on the post-hoc dataset. Input uncertainties for Taylor series expansion and the MCS are specified in Table 3.1. All MCS had 10,000 perturbations per data point. This example probe is stalled at a cone angle above 45°, so all data above 45° is ignored.

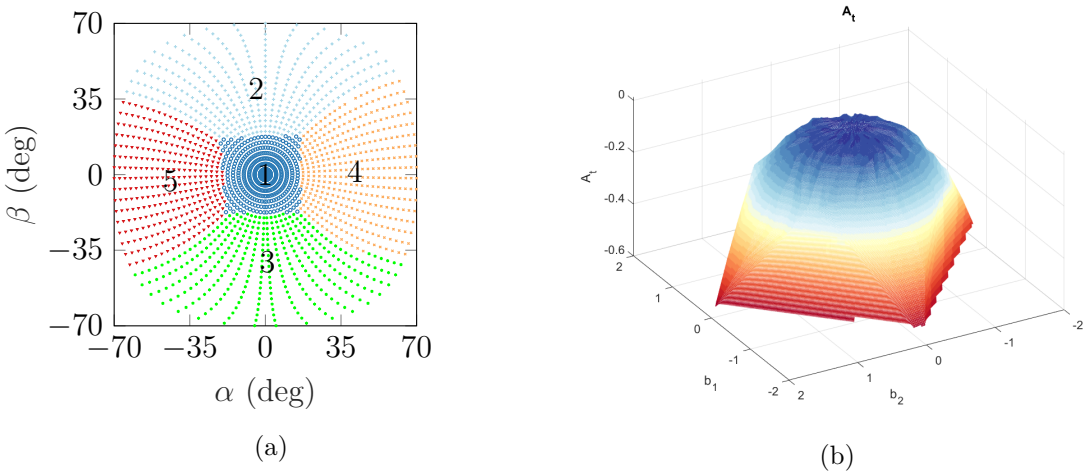

(a) (b)

Figure 3.7: (a) Local interpolation scheme with each sector marked with the port number of the highest reading and (b) the total pressure coefficient A_t in the sector with port number one.

First the linear approximation of the Taylor series method is evaluated by comparing the results to a corresponding MCS. The evaluation is implemented for the calibration process where the integration function is created. The results of this comparison are shown in Fig. 3.8 where the Taylor series is named Taylor S. and MCS is the MCS_1. For lower cone angles, the Taylor expansion slightly underpredicts the uncertainty compared to MCS_1. The slight difference indicates that the linearity of the Taylor series is satisfactory. However, at a cone angle of 20°, results from the MCS have a local maximum that is not captured by the Taylor series. The local maximum at a cone angle of 20° can be explained by calibration perturbations propagated through the interpolation function in the MCS while not in the Taylor expansion method. The interpolation function changes sectors at a cone angle of 20° and is where the gradients are highest. Hence, any perturbations in b_1 and b_2 can affect sector selection and therefore significantly affect the interpolated value, which is only captured in the MCS and not in the Taylor series analysis. Therefore, Taylor series are likely to produce reasonable total individual and error estimates on the interpolation function.

The errors introduced in the measurement processes was assessed by a second MCS_2 excluding uncertainties from the calibration process. Thus, the only difference between the second MCS_2 and the first MCS_1 is where the perturbations are introduced. The result from this simulation, MCS_2, is shown in Fig. 3.8 as a dashed black line with dot markers. Compared to errors introduced in the calibration process, errors from the interpolation functions are more profound for cone angles less than 2° and unexpectedly low near a cone angle of $\approx 15 - 30°$.

Each individual probe has a calibration point where the absolute port pressures is the lowest. Since the permutation scales to the port reading magnitude, this calibration point should also have the smallest permutations. For the 5-hp probe used in this example, the minimal port pressures occur at a cone angle of $25 - 35°$ and maximum at a cone angle of 0°. From equation (3.4) one can appreciate the effect of

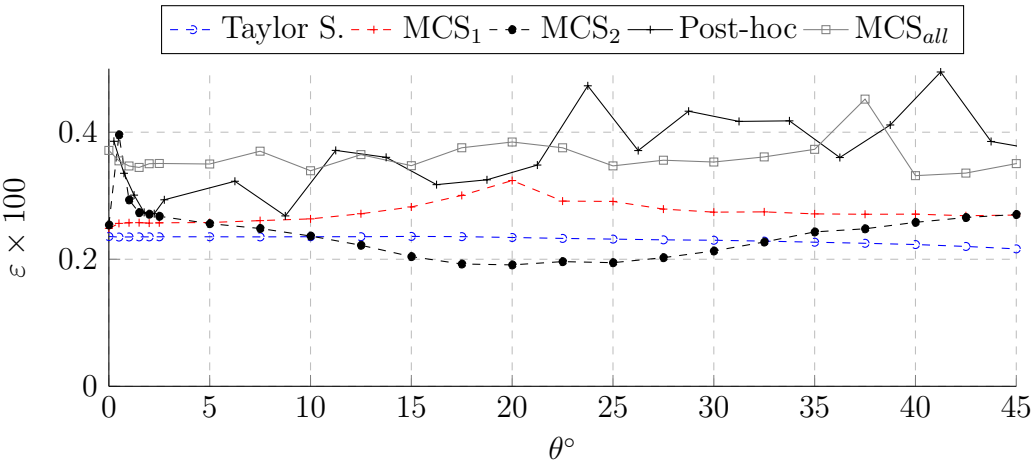

Figure 3.8: Comparison of estimations of using Taylor series, Monte Carlo simulation and a post-hoc error estimation check.

high magnitude perturbations on the total pressure measurement where both P_i and q_c are scaled to peak port pressure. From observing the results of MCS_2 in Fig. 3.8, the more profound errors at low cone angles can be derived from a combination of large introduced perturbations in (3.4) from P_i and q_c, together with the rather noisy total pressure coefficient A_t at a low b_1 and b_2, as seen in Fig. 3.7b. Lower port values P_i are reflected in the reduced uncertainty for cone angles between 20° and 30° countering the effects from the high gradients in A_t at this location.

One potential criticism of the MCS_2 could be that the perturbations were performed near each calibration point and do not capture errors at measurement between calibration points. Therefore, an identical MCS was performed on the post-hoc calibration dataset but using the baseline interpolation function. The MCS using post-hoc data with the baseline function yielded nearly identical results as the baseline dataset with the baseline interpolation function and is not shown here.

With effects from isolated permutations in the calibration and measurement better understood, a complete system MCS was performed. The result from such simulation is shown in Fig. 3.8 and marked with MCS_{all}. A robust way to validate the MCS_{all} is to use the post-hoc dataset with the baseline interpolation function and control each datapoint against the reference value provided by the calibrator. Since the calibrations are performed directly after one another and without hardware changes, this comparison mitigates long-term bias errors, transducer bias errors and probe misalignment effects and effectively provides a minimal level of expected uncertainty. The result from such a post-hoc error estimation is shown in Fig. 3.8 and is marked as Post-hoc in the figure. There are notable similarities between MCS_{all} and the post-hoc data, even though the post-hoc results are more scattered. The higher scattering of the post-hoc data can be attributed to an order of magnitude higher variance for each cone angle in the post-hoc data, which in part can be attributed to the substantially smaller sample size. Another reason for the higher variance in the post-hoc data compared to MCS_{all} is due to the Gaussian perturbation model. The Gaussian perturbation model utilised does not capture real-world effects such as

random sensor biases, time-dependent variations or aerodynamic imperfections of the probe or the flow.

The general similarity between the post-hoc and MCS_{all} does, however, indicate that the Gaussian perturbation model represents a large part of the real-world input errors.

From the observed MCS results and post-hoc data of the current probe configuration and operational conditions, an upper estimation of the interpolation error is in the order of 0.15-0.25% for most of the dataset. This is a heuristic estimation limited by the lower detection range of the calibrator. A lower value is plausible if not expected if a higher rate of transducer noise can be mitigated or if data from more controllable environments are used, for example, numerical simulations or potential flow as in [39].

An example of the limitation of the calibrator can be found in cases near parallel flow. At this angle, the centre port perceives the highest pressure throughout the calibration and measurement. In Eq. (3.5) and Eq. (3.3), with a high centre port pressure, errors introduced by P_i become dominant for both the total pressure coefficient A_t and q_c. The error introduced from the PSI-9116 to produce one measurement would then be in the order of $\varepsilon P_t \approx \sqrt{\delta P_t + \delta P_t + \delta P_t} \approx 1.73\delta P_t = 0.26\%$. The assessment above excludes any other effects from noise from the transducers.

Measurement Considerations

There are a few considerations other than typical free-stream flow effects when using a MHP, such as viscous or compressible effects. Any pressure measurement using a pneumatic probe in flow measurement is intrusive and might change the flow field, and the smallest feature resolvable is the diameter of the port. Chernoray and Hjärne showed in [11] that any pressure gradient across a MHP will proportionally offset the measured flow angles from the actual and presented a correction for this effect. As the probe is used in highly turbulent flow in the TRS and ICD, turbulence must be considered. Turbulence causes an overestimation of the measured mean port pressure. For an ideal case, this can be derived from a Reynolds decomposition of the Bernoulli equation and by introducing isotropic turbulence. By rewriting the expression to be dependent on turbulence and defined in $\sqrt{v'^2}/V = Tu$, an indication of the effect from turbulence can be estimated.

$$P_{tot} = P_s + 0.5\rho(V^2 + \langle u'^2\rangle + \langle v'^2\rangle + \langle w'^2\rangle) = V^2(\sqrt{1 + 3Tu^2}) \tag{3.6}$$

The highest value of free-stream turbulence measured in the facility was 6%, which inserted in Eq. (3.6) causes a 0.5% offset on measured total pressure. However, the turbulence downstream of the rotor is not isotropic and the effect of turbulence on a MHP is still largely undocumented, as stated by Tropea and Yarin [52]. Scribner [48] conducted an isolated study where no noticeable effect from turbulence below an intensity of 8% was found.

Large-scale fluctuations are present in the TRS; thus sampling time must be considered. This is case specific to each set-up and measurement point. Both Borja [42] and Axelsson [3] selected a few representative points and studied the effect of

sampling time. As the uncertainties in the MHP are highly dependent on the port pressure accuracy, this needs to be thoroughly studied for each new flow field.

Implementation in the TRS

For the data in the attached papers, the TRS is instrumented with two MHPs; one 5-hp to traverse the inlet boundary and one 7-hp to study intermediate and outlet planes. In Fig.3.5b, the general set-up and flowchart for processing pressure measurement are shown for the TRS.

For the MHP implemented in the TRS, an uncertainty expression for each measurement point was derived. The uncertainty in the formulation of the interpolation function and measurement processes was estimated using Taylor expansions with typical values for the 5-hp shown in Table 3.2. Uncertainties from 0.2% were added to interpolation functions using RSS as shown in Eq. (3.7). The error for each measured point is now defined analytically and can be repeated for each measurement point and plane average uncertainty.

$$\varepsilon_{A_t} = \sqrt{(\varepsilon_{A_{t_{Cal}}})^2 + (\varepsilon_{A_{t_{Meas}}})^2 + (\varepsilon_{A_{t_{Interp}}})^2} \tag{3.7}$$

Figure 3.9a shows the total pressure on the outlet of the TRS at ADP and Reynolds Number of 235,000. In Fig. 3.9, the corresponding total pressure error is shown for the same dataset.

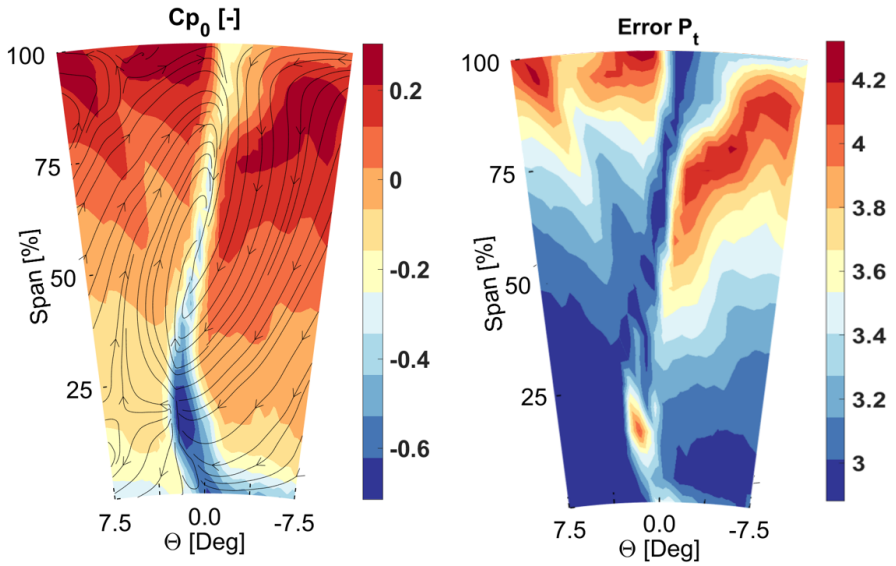

(a) (b)

Figure 3.9: (a) Total pressure at the outlet plane of the TRS at ADP and (b) estimated total pressure error outlet plane of the TRS at ADP.

Uncertainty Mitigation

For the conditions found in the TRS, one of the principal limitations of the accuracy of the MHP is the error introduced from the transducers. This is especially important

with total pressure measurement as the dynamic pressure is high, but the sought differential total pressures are low. The introduced errors are generally proportional to the perceived pressure, and by selecting a reference value more suitable for the measurement campaign, the magnitude of the introduced error can be reduced. In this case, a value to bring the MHP port reading closer to the expected inlet-outlet differential total pressure readings is more suitable.

The static pressure coefficient can be utilised to estimate the minimum suitable transducer pressure range. Consider the flow around a semisphere with the free stream static as transducer reference to represent a multi-hole probe. The C_p value would be in the range of one to minus one, with some variations on the aftward side from losses and local acceleration/separations. At the stagnation point, the value would be 1 with values around $C_p - 1$ or lower on the acceleration peak. If, instead, the total pressure from the Prantl tube in the free stream is used as the reference, the stagnation point will now have a pressure coefficient $C_p \approx 0$ while suction peak $C_p \approx -2$. In the ideal case, this would be worse for accuracy as it would require twice as large FS for the traducers. In practice, transducers are available in a set of ranges, and the transducers in the TRS are used to $\approx 50\%$ of FS at peak velocities. A conical multi-hole probe mounted in the TRS using the room pressure as a pressure reference has a pressure coefficient of $-1.6 \leq C_p \leq 1$ for angles up to cone angles of 70° and $-1.04 \leq C_p \leq 1$ for angles up to 45°. A change of transducer reference to the reference probe can therefore be implemented without the risk of overloading the transducer. The estimated improvement by changing the reference pressure is illustrated in Fig. 3.10 using the same procedures as in Fig. 3.8 but changing the transducer reference closer to the expected quantity. The blue curve indicates a MCS similar to the presented in Fig.3.8, and the red shows a MCS after the reference change. The introduced perturbations are Gaussian with a minimum limit of 0.6 Pa to replicate the PSI-9116 characteristics of $0.15\%R \pm 0.6Pa$. Figure 3.10 shows that there is a substantial gain in accuracy of total pressure measurement to be had when changing the reference in TRS.

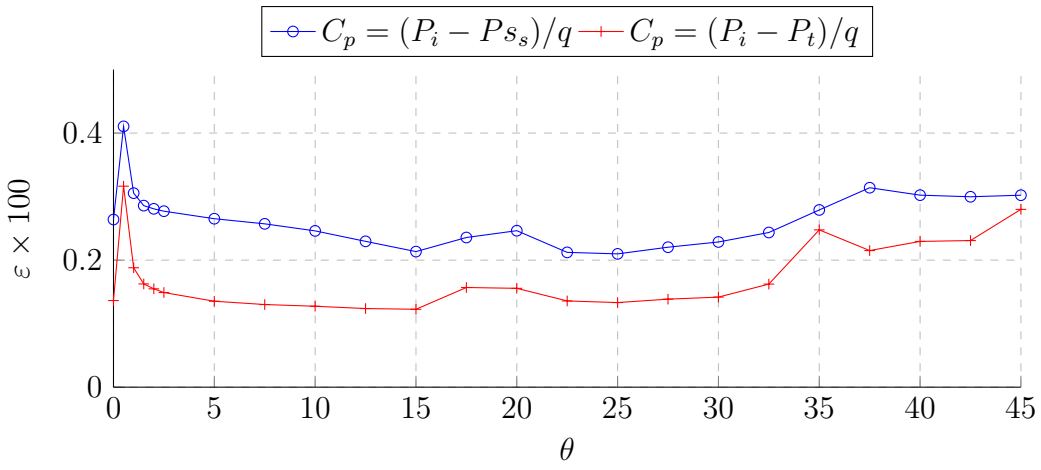

Figure 3.10: Comparison of the effect of changing pressure reference to the MHP, using a MCS to estimate the effect.

3.3.2 Heat Transfer

The heat transfer measurement performed in this work primarily aims at measuring the convective heat transfer h between aero surfaces and the fluid. In Eq. (3.8), convective heat flux is represented by q''_{conv}, surface temperature by T_w and free stream air temperature as T_∞. This chapter focuses solely on methods utilising IR-thermography to measure the surface temperatures.

$$q''_{conv} = h(T_w - T_\infty) \tag{3.8}$$

At first glance Eq. 3.8 looks uncomplicated. However, in comparison to other measurements, heat transfer measurements generally struggle to achieve acceptable accuracy. The measurement principle of heat transfer is simple; a temperature difference is created to achieve a heat flux, the temperatures are measured and h can be calculated. The key challenge is the multidisciplinary nature required to isolate all of the components from interaction with the environment.

Steady State Heat Transfer

The steady-state convective heat transfer measurement performed in this work is achieved by manufacturing a plastic model by SLA with internal water channels. In the water channels, hot water is circulated. The plastic model acts as an insulation layer around the heated core.

The conjugate heat transfer between the ambient air, isolated plastic wall and inner water channel is solved to deduce the convective heat transfer coefficient. To measure the convective heat transfer, the radiative heat flux must be isolated or preferably minimised. The estimation of the radiative part is often the most problematic to measure but was made possible by using a modified version of the reflective marker array (RMA) method as formulated by Kirollos and Povey [27]. Figure 3.11 shows the general set-up of the measurement with the accompanied main thermal fluxes, defined in Eqs. (3.9) to (3.11). To the left in Fig. 3.11 is an instrumented vane and to the right is a one-dimensional representation of a cut-out section of the vane wall. Magenta arrows symbolise heat fluxes and there are four indexed positions in Fig. 3.11. Variables that are sub-indexed with 1 are related to the inner wall values. Inner wall temperature is T_1, inner wall heat transfer coefficient h_1 and average water temperature T_1^∞. Sub-index 2 relates to surface properties, such as temperature T_2 and emissivity ε_2. The surface uses coatings of two types; leaf gold $\varepsilon_{2,1}$ and a black Nextel paint, ε_2. Sub-index 3 is for air properties, and group b is for background properties. σ is the Stefan – Boltzmann constant, t is the shell thickness and k thermal conductivity.

$$q''_{cond} = \frac{k}{t}(T_1 - T_2) \tag{3.9}$$

$$q''_{conv^{H_2O}} = h_1(T_{1\infty} - T_1) \tag{3.10}$$

$$q''_r \approx \sigma\left(\varepsilon_2 T_2^4 - \tau_3 \varepsilon_b T_b^4\right) \tag{3.11}$$

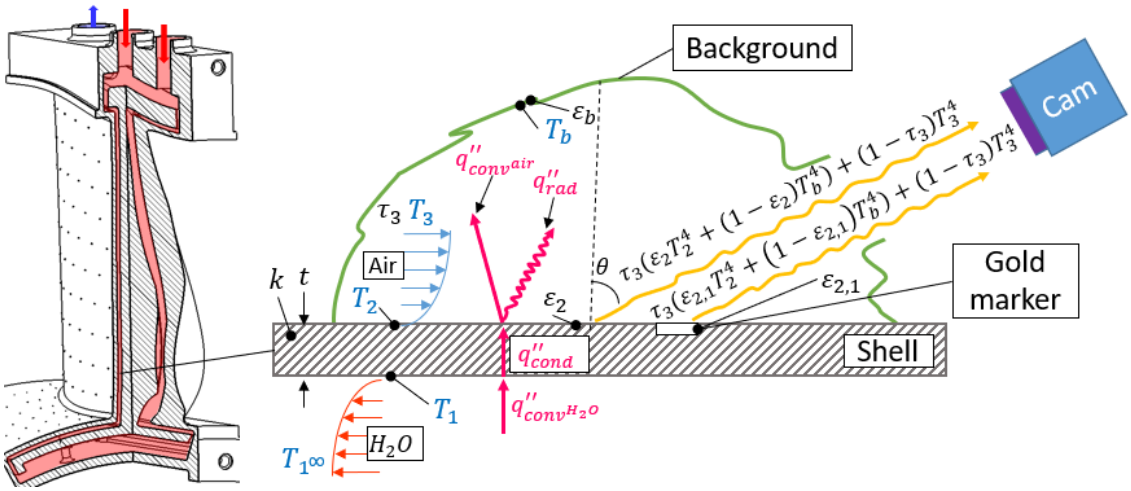

Figure 3.11: Schematics of the instrumented heat transfer OGV together with a one-dimensional simplification.

Using conservation of energy with Eqs. (3.8) to (3.11) and solving for convective heat transfer coefficient on the air side h_2 provides Eq. (3.12).

$$h_2 = \frac{q''_{cond} - q''_r}{(T_2 - T_3)} = \frac{1}{(T_2 - T_3)} \left(\frac{k}{t}(T_1 - T_2) - \sigma \left(\varepsilon_2 T_2^4 - \varepsilon_b T_b^4 \right) \right) \tag{3.12}$$

As mentioned, the challenge of heat transfer measurements is, in general, to isolate interference with ambient conditions. A fluid core with plastic isolation has several potential interactions, both with internal and external factors.

Measurement Procedure

Figure 3.12 shows the data flow and processing when performing a surface temperature measurement and general steps to calculate the heat transfer coefficient h_2. The green area marks the calibration procedure. The red shaded areas mark the measurement processes to the point where reliable surface and background temperature have been defined. The red box *External* is external material and geometrical errors, which are included in the error estimation. Errors introduced outside the coloured areas such as geometrical translations or Fenit Element Method (FEM) calculations are challenging to estimate analytically but are estimated later. Before measurements, the camera counts X are correlated to surface temperatures, view angles θ, focal settings and more. The calibration includes a non-uniformity compensation (NUC) and a polynomial function. When the camera is used during measurement, the counts are converted to surface temperature readings. As the camera sensor is sensitive to the temperature of the optics and the temperature of the surrounding air, an in-situ correction is applied using a PT-100 temperature sensor T_{is}, which is coated in the same material as the test object. The heat transfer coefficient h_2 is first calculated assuming one-dimensional wall heat flux and T_2 as surface temperature. Later in the process, the effective wall temperature T_w and the effective background T_r temperature are calculated using the RMA method. The one-dimensional heat

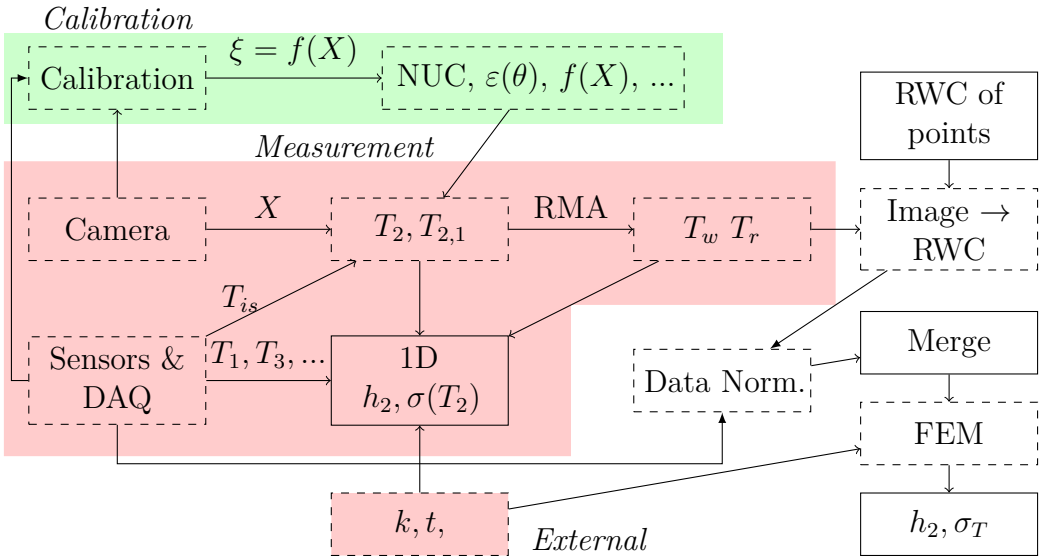

Figure 3.12: Steady state heat transfer measurement flowchart. Dashed boxes illustrate introduced errors in the process.

transfer coefficient is calculated again using T_w and T_r to assess the effect from the RMA method. The temperature images are mapped to real-world geometries using the gold markers on the surface of the OGV. As several fields of view are necessary to capture aero surfaces of the OGV several sets of heat transfer results are normalised and merged. FEM simulations are used with the normalised surface, ambient and core temperatures to calculate the in-wall heat flux. The heat flux from FEM calculations is later subtracted by the calculated radial heat flux and inserted in equation (3.8) with T_r and T_w to provide the convective heat transfer.

The order of magnitude of the errors introduced in the spatial conversion of images, data normalisation and FEM calculations is provided by the difference of the one-dimensional approximated results and results provided by the FEM calculation. The most significant discrepancy was found at the highest temperature gradients at the laminar-turbulent transition on the suction side. The deviation was in the order of $1-2\%$ with a single-pixel value of 3%. The errors introduced in the FEM calculations are expected to be a portion of the full effect and are estimated to be negligible. The $1-2\%$ errors include the normalisation process to the dataset variation. Higher variations have been observed in unpublished work when the test was performed while assessing ageing and moisture effects on the SLA material properties. The geometrical errors introduced from mapping the image to real-world coordinates are outside the scope of this thesis.

Figure 3.13 shows an flowchart of the process from left to right. To the left is a photo of the OGV coated with Nextel paint and gold markers. Next in the centre is the surface temperature T_2 shown after the markers have been filtered out. Further along is the effective background temperature T_r and surface wall temperature T_w. Most rightward is an isometric view of the unstructured mesh for the FEM simulation.

Transient Heat Transfer

The IR-thermographic data for the steady-state heat transfer study used an average of 1000 images. The averaging of the signal mitigates statistical uncertainty from the camera signal and removes any time-dependent temperature fluctuations caused by variations in the flow field. Using the same raw data for the steady-state and studying the time domain, unsteady flow features can be detected.

There are limits to what size of transient features can be detected based on the thermal capacity of the surface, camera noise levels and camera time resolution. The capacity of the surface can either delay or completely dampen away features that are either too short-lived or too weak to cause a sufficient cooling effect. The camera background noise, referred to as Noise Equivalent Temperature Difference (NETD), is, in better cases, around 10–20 mK for the Phoenix 320. The maximum full-frame sample frequency for the Phoenix 320 is 120 Hz, but 50 Hz was used for all experiments.

The basic principle for laminar-turbulent transition or separation detection, independently if the standard deviation of the temperature signal σ_T or differential IR-thermography (DIT) defined in Raffle et al. [38] is described in this paragraph. A laminar-turbulent transition is accompanied by formation of stochastic turbulent streaks. Each turbulent streak causes an increase in skin friction and heat transfer locally, which is reflected in the surface temperature. If these fluctuations are of sufficient magnitude to be detected, the amplitude of the temporal standard deviation σ_T can reveal their location as shown in [41]. The temperature deviation cannot alone reveal the mode of transition or if a separation occurred. Only with complementary observation can the method be tuned to detect a certain kind of flow feature. As a rule, significantly higher and larger temperature fluctuations are observed at separated flow [40] compared to laminar-turbulent transition. In Paper D, the detection of the laminar-turbulent transition by σ_T is verified at midspan on the suction side of an OGV by hot-wire measurements. The method and results are discussed in detail in Paper D. DIT can provide further information since individual streaks are detected and traced, often by sliding frame subtraction (SFS). For studies in the TRS, the relation between camera sampling speed, object size and flow velocity makes this method unfeasible.

A portion of the field of view is lost when projecting the raw images on the OGV

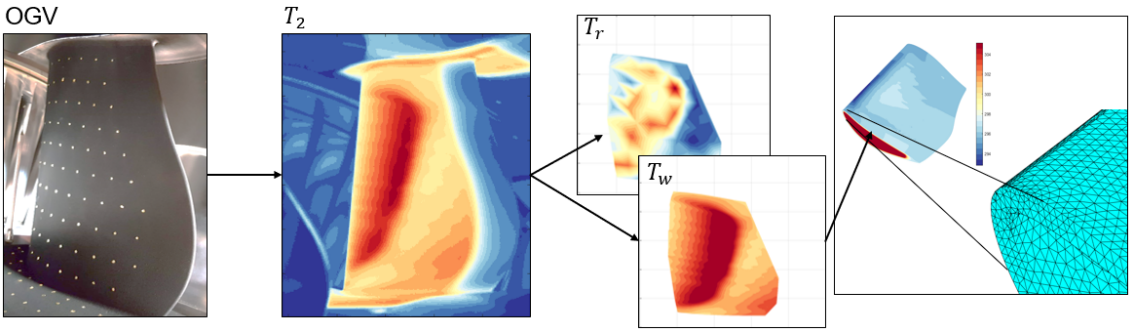

Figure 3.13: Flowchart showing processing of average IR-Thermography data

surface in Papers C and D. With a larger field of view available in the raw images, these are occasionally better to qualitatively illustrate flow features. The methods described above are implemented on raw images on a camera view of OGV in the TRS, which are shown in Fig. 3.14. The flow enters from the left in Fig. 3.14, and thick black lines mark the leading and trailing edges. There is no heating downstream of the red dashed line, and all figures share the same colorscale. In Fig. 3.14a, σ_T is shown for ADP, which is the same ADP as in Paper D. The verified location of the laminar-turbulent transition in the TRS is marked with A. The roll-up vortex is marked with C in Fig. 3.14a. Figure 3.14b illustrates the same view as in Fig. 3.14a but for a case with substantially increased blade loading. As expected, the corner separation marked with B in Fig. 3.14b has a more eminent σ_T compared to observation of transition in Fig. 3.14a. In Figure 3.14c, the sliding frame subtraction (SFS) is able to capture individual streaks and transient features on the surface, but with the Phoenix 320 camera sample rate at 50 Hz, the temporal resolution is insufficient to provide any further information compared to σ_T.

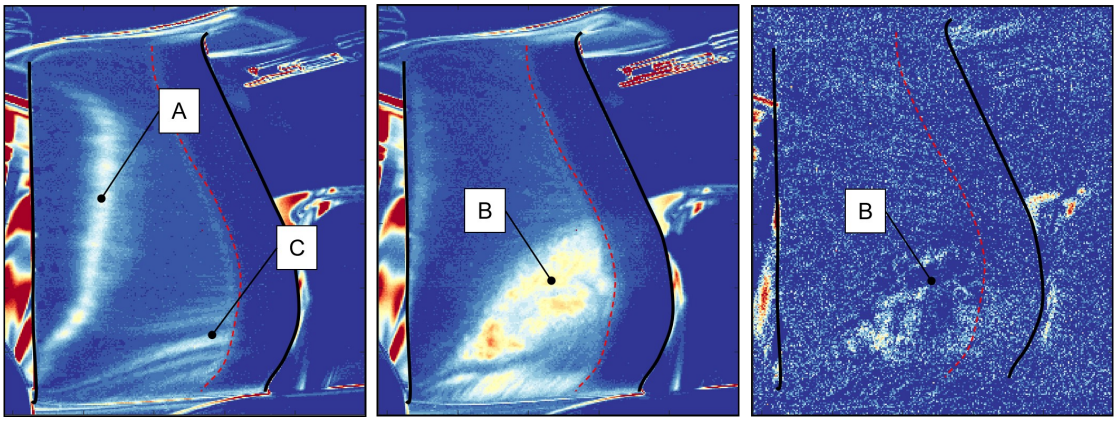

(a) σ_T at ADP (b) σ_T at ADP+15 (c) SFS at ADP+15

Figure 3.14: Example of advanced analysis of IR data for laminar-turbulent transition and flow separation at Re=235,000: (a) σ_T for case with transition; (b) σ_T for case with separation; and (c) SFS for case with separation.

3.4 Experimental Results in the TRS

The results from the TRS were gathered over a diverse set of projects, and whilst Chapter 2 provides a general description of the flow field and typical challenges, the relation of these to the results might not be obvious. Therefore, this section complements Chapter 2 and aims to tie the diverse results in an overarching manner for the reader.

As described in Chapter 2, the TRS operates in conditions such that a substantial amount of the leading edge can either be laminar or turbulent depending on the operational conditions. Both the mode and location of the laminar-turbulent transition can significantly impact the aero performance of the OGV. The effects from surface roughness are considered secondary for the transition onset [33] but during the

lifetime of an engine, surface roughness typically increases as a result of deterioration and contamination. Since this could affect the transition onset, effects from surface roughness were experimentally investigated for the TRS by spanning a range of surfaces and operation points in Paper A. For a reasonable level of roughness, the effect was predictable with increased wakes width and pressure losses in correlation with surface roughness. However, a surface roughness outside typical values in a TRS triggered a rapid pressure drop when increasing the Reynolds number from 235,000 to 465,000. The rapidly increased pressure was predominantly found near the hub, indicating a corner separation. Corner separations are notoriously challenging to replicate numerically and were only partly successfully captured in numerical RANS simulations performed in both CFX and Fluent using $k-\omega$ model with standard settings on the transition model $\gamma - Re_\theta$. The experimental studies until this point had been performed using pneumatic measurements such as MHP, pressure taps and wake integration to quantify the aerothermal performance. The author noticed relatively relatively large amounts of noise when calculating the integrated total pressure losses in the TRS. A need to reduce the introduced noise in the MHP method was identified, which initialised the error mitigation of the multi-hole probe method described in section 3.3.

Flow visualisation was performed to provide further insight into flow features on the suction side of the OGV and is shown for the suction side at ADP and at a Reynolds number of 235,000 in Fig. 3.15. Green lines indicate flow pathways observed from filming the experiment, and the area marked with A surrounded by green dashed lines is an area with slow movements and large droplets. One can observe the corner roll-up vortex traverse upwards along the span as the stream tubes expand downstream. The location of the corner roll-up vortex observed in the flow visualisation correlated to the dominant losses observed in the wake studies. In Fig. 3.15, the spanwise redistributed flow is lesser near the shroud compared to the hub and agree well with a hub loaded OGV. A much smaller secondary flow influence near the shroud indicates that the tip leakage has a negligible effect on the baseline OGV performance for this configuration. As a side note, the corner roll-up vortex expands further along the span with increased blade loading, later shown in Fig. 3.17.

Observation of the flow visualisation between the green dashed lines in Fig. 3.15 indicates a region with reduced skin friction revealed by the accumulation of pigment. In combination with the location and conditions found on the OGV suction side, the reduced skin friction provides a weak indication of a bypass laminar-turbulent transition or a separation induced transition.

The convective heat transfer was primarily measured to assess the thermal loads on the OGV but also to provide further insight into flow features. An overview of the heat transfer methods implemented in the TRS is described in section 3.3.2. A substantial amount of work was employed to improve earlier measurement methods, partly presented in Paper C. The convective heat transfer coefficient on the OGV is shown in Fig. 3.16 at ADP and a Reynolds number of 235,000. The data has been unfolded along the OGV leading edge to visualise both sides. The suction side is marked with SS and the pressures side with PS. In Fig. 3.16, along midspan

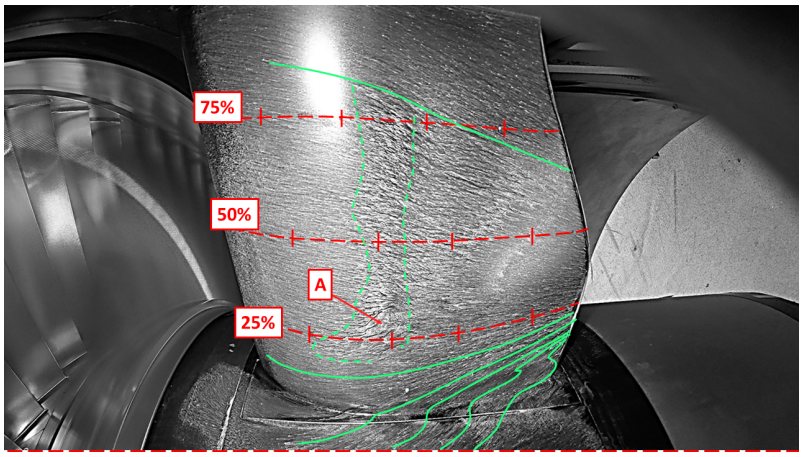

Figure 3.15: Flow visualisation of the suction side of an OGV at design conditions and Reynolds number 235,000. Green lines indicate flow path of the pigmented fluid, and red lines indicate the different spans along the OGV.

on the suction side, the heat transfer reduces downstream from the leading edge until a rapid increase occurs. This is the typical heat transfer history of a laminar boundary layer developing and transitioning to a turbulent boundary, and the trend is expandable for most of the span. The spanwise regions of reduced heat transfer rate correlate well with the reduced skin friction observed in the flow visualisation. In addition, impacts from the roll-up vortex can be detected by the reduced heat transfer near the lower aftward side of the suction side.

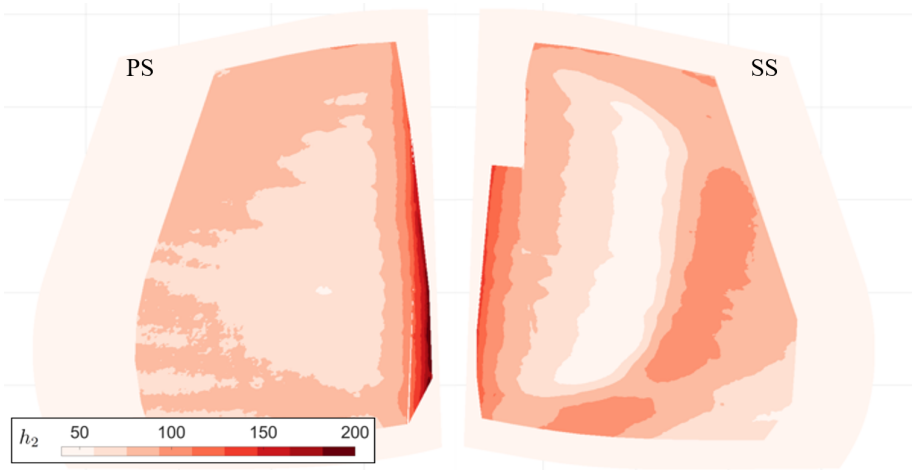

Figure 3.16: Heat transfer coeffecient h_2 on the pressures side (PS) and the suction side (SS) of the OGV at ADP.

The already available raw data from the steady-state heat transfer contained the surface temperature fluctuations, which can be used to detect transition or separation location by σ_T as described in section 3.3.2. Figure 3.14 shows a raw image processed to display σ_T for an OGV, and Fig. 3.17 shows the same results but translated and projected on the suction side of an OGV as blue contours. Both Fig. 3.17 and Fig. 3.14 show the transition location and roll-up vortex. In the projection process,

the raw image is trimmed and the roll-up vortex coverage reduced. The transition's location could be defined with relatively high certainty as to the flow-visualisation and the two IR-thermographic methods indicating the same location. Neither of the beforementioned methods can identify the transition mode required for the verification data. Boundary layer studies by hot-wire are a well-established method that can detect the transition mode but are onerous to perform on a large, vibrating, double swept surface. A pragmatic solution was to verify the transition at selected locations and the transition mode was expanded by the similarity to σ_T and h.

Figure 3.17 shows a compilation of numerical and experimental results on the suction side of the OGV for three load cases at a Reynolds number of 235,000. Blue contours indicate the experimental observed laminar-turbulent transition location, the numerical simulations by dashed black lines, streamlines from flow visualisation as red lines and numerical streamlines as solid black lines. For all cases the numerical results predict an earlier laminar-turbulent transition than the experimental data and overestimate the secondary flow structure. The overestimated secondary flow structures are also reflected as larger low-pressure zones near the hub in the wakes, shown in Papers A, B and D. The most significant discrepancy of transition location between numerical and experimental results is for the high blade loading case ($\phi = 0.657$). At the location with the most significant discrepancy is a dashed red line in Fig. 3.17c. The dashed red line illustrates a cross-flow observed while running a rich flow visualisation mixture, indicating a zero spanwise pressure gradient and a probable separation bubble. Further supporting a small separation bubble is the pressure distribution presented in Paper D, where a halt in pressure recovery for this load case at the chordwise of the cross-flow can be observed. A halt in a pressure recovery on the suction side of an airfoil is a common indication of a small separation bubble.

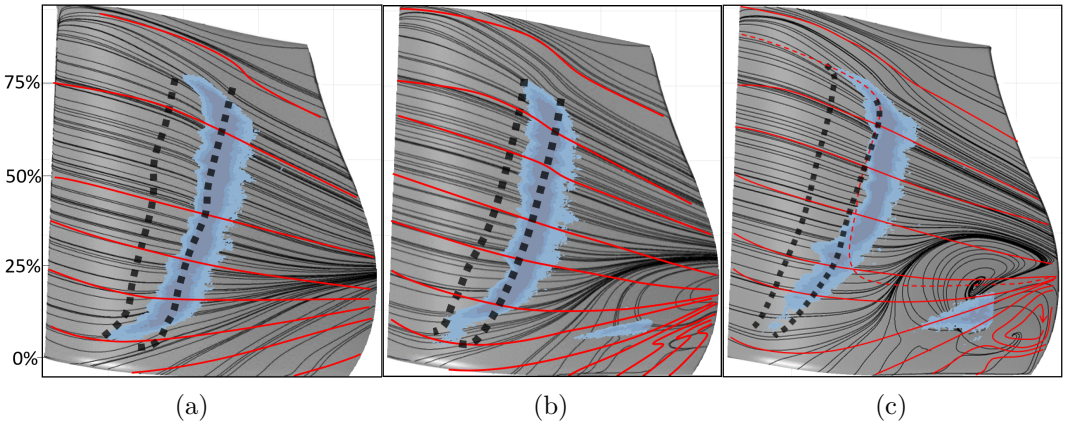

Figure 3.17: Experimental detection of laminar-turbulent transition (blue shaded area) compared to numerical results (black dashed lines) together with numerical (black lines) and experimental stream lines (red) on the suction side of an OGV for three flow coefficients at a Reynolds number of 235,000. See text for further details.

The typical utilisation of verification data in the laminar-turbulent onset location would be to tune the transition model SST ($\gamma - \theta$) or turbulence intensity at transition

until the onset matches. However, before tuning any model, the input parameters are investigated. Transition models such as the SST $(\gamma - \theta)$ [34] are in large part based on correlations such as the one by Mayle [33] and Praisner [37]. These correlations are derived from a large dataset of investigations in test facilities of various turbomachinery and are based on the momentum thickness Reynolds number Re_θ as defined in Eq. (3.13), some version of the acceleration parameter K_θ and turbulence intensity Tu. The laminar-turbulent transition onset occurs when the local momentum Reynolds number exceeds the critical momentum Reynolds number Re_{θ_t}. The correlation for the onset are case dependent but for flows with relatively high turbulence Mayle suggested $Re_{\theta_t} = 400Tu^{5/8}$, but correlation to secondary effects such as surface roughness are also available, see Eq. (4.3).

$$Re_\theta = \frac{U_\infty \theta}{\nu} \tag{3.13}$$

The momentum thickness θ, free-stream velocity U_∞ and the kinematic viscosity ν are used to defined Re_θ. The acceleration parameter is defined by the velocity at the edge of the boundary layer U with the partial derivative $\partial U/\partial s$ along a surface line s. The kinematic viscosity is defined from properties in the free stream if not otherwise stated.

$$K = \frac{\nu}{U^2}\frac{\partial U}{\partial s} \tag{3.14}$$

Turbulence intensity has been measured throughout the test section via hot-wire and can be used as verification data. The boundary layer measurements provide the momentum thickness Reynolds number Re_θ and static pressure distribution can be used to calculate the acceleration parameter K_θ. The same quantities can be extracted from the numerical simulations, and instead of matching transition onset location, the input parameters are compared.

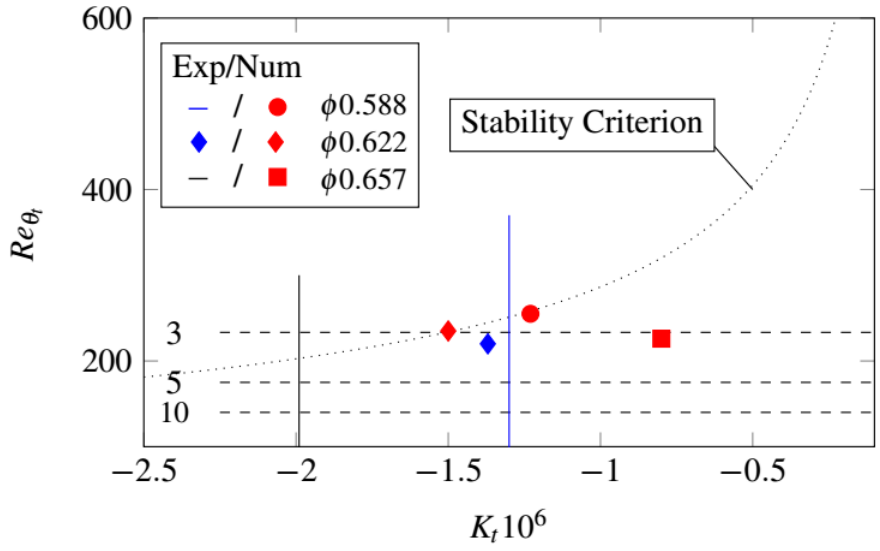

Figure 3.18: Momentum thickness Reynolds number at transition onset Re_{θ_t} and acceleration parameter K for the three numerical and experimental cases

The results are shown in Fig. 3.18 with the momentum thickness Reynolds number at transition onset on the vertical axis, and the acceleration parameter on the horizontal axis. The momentum thickness at transition is only known for one of the experimental cases at ADP, but one can observe that the range for momentum transition location for all cases is relatively narrow around the expected 220 for the observed 3% turbulence intensity at the transition onset. The most significant discrepancy is observed for the highest blade loading $\phi = 0.657$. The numerical results are outside Tweights stability criterion, indicating that separation is likely to occur if the boundary layer is laminar. The acceleration parameter for the experimental results is at the opposite extreme.

The observation of Fig. 3.17 and Fig. 3.18 indicates that the transition SST $(\gamma - \theta)$ transition model is is, for the presented case, predicting the boundary layer state at transition onset correctly. The large discrepancy in location at the high blade loading locations is likely due to the failure of the numerical simulation to capture a separation induce transition, which is unlikely to have been corrected by tuning the transition model.

Chapter 4

Low-Pressure Compressor Test Facility

This chapter presents the general design of the newly constructed compressor test facility. The chapter also expands on a few selected features that the author considered important from a practical aspect, not yet published or unlikely to be included in future publications. Paper E provides general aspects of the facility's design, while Paper F adds details of the pre-testing evaluation of the LPC.

4.1 General Description

The facility is built as part of the Horizon 2020 ENABLEH2 project and is constructed in the Chalmers Laboratory of Fluids and Thermal Sciences. The principal purpose of the facility is to experimentally evaluate the ICD's ability to synergistically be utilised as a heat exchanger in cryogenic fuelled engine concepts. Thus, the facility is designed to evaluate engine-typical ICDs as well as novel synergistic ICD heat-exchanger concepts.

The facility is a vertical annular 2.5-stage low-speed compressor rig and built for continuous operation at a wide operational range of Reynolds numbers and pressure ratios. The general layout of the facility can be seen in Fig. 4.1 where the two-stage compressor drives the main flow in the facility. Operational conditions are achieved by restricting the flow with a restrictor upstream of the LPC and regulating the compressor's input power. The flow is conditioned for thermal and pressure uniformity in a combined volute and flow conditioner between the restrictor and the compressor inlet. The ICD is mounted downstream of the two-stage compressor, and the ICD outlet is the outlet of the facility. The flow is recirculated into the facility in the return duct for thermal stability and to limit particle and noise mitigation between the laboratory and the facility.

The LPC consists of 75 adjustable inlet guide vanes (IGV), rotor 1 with 61 blades (r1), 124 stator blades (s1), rotor 2 with 69 blades (r2) and finally, the OGV with 126 stators. The LPC design is derived from a slightly updated version of the VINK LPC presented in Lejon et al. in [30]. Fundamental aerodynamic and geometrical design similarity was targeted with the limitations of the lab and available instrumentation

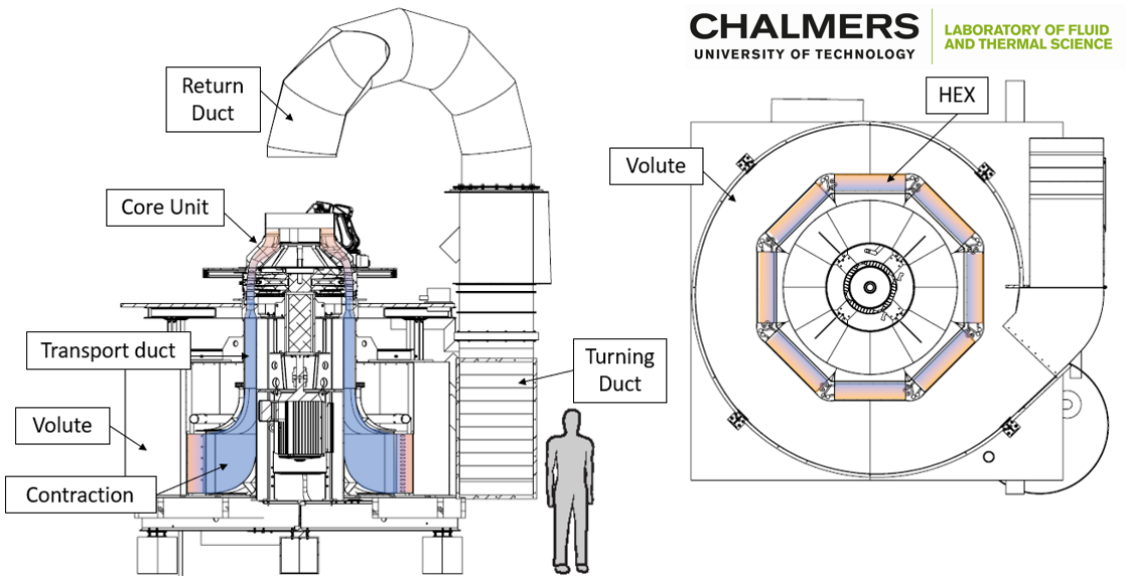

Figure 4.1: Schematics of Chalmers low-pressure compressor facility.

constraining the design. The LPC and ICD designs were iterated with these initial targets and constraints between the experimentalist and the aerodynamic designer. The final aerodynamic design of the LPC was performed at GKN using both in-house design methods and methods similar to presented in [30]. Section 4.1.2 elaborates on the rationale mechanical and aerodynamic design choices of the LPC.

The facility's design can be divided into two groups, of which the first relates to the core flow components, such as the LPC and the ICD. The secondary group is all systems that support the first group, such as mechanical structure, cooling and manufacturability. This thesis focuses on the former group, and the following section describes the design along the flow path from the inlet to the outlet. The latter group is briefly covered in the thesis but primarily aimed to improve operation, simplify assembly, and enable access the ICD and compressor. All parts were designed to have a safety factor above three for a five-year normal operation period. Time allocated for the design of these subsystems was based on the impact of failure from a qualitative risk assessment. Hence, the outer structures were assessed with hand calculations and classic beam correlations due to the low impact of failure, while structures, such as the LPC mount, were extensively simulated for both dynamic and static loads using the mechanical workbench in Ansys^{TM}.

4.1.1 Design of Flow Conditioning Unit

Industrial jalousie dampeners enable simple control of the mass flow upstream of the LPC. However, the outlet flow from such a device is highly non-uniform and not suitable for the compressor inlet as axial compressors are sensitive to blade flow angles and inlet flow distortions. The propagation of inlet distortions for a transonic compressor of 20% in total pressure through several stages was investigated by [31]. Even though some dampening effects were observed, a substantial part of

the distortions propagated through the compressor. Local and large distortion will interfere with performance evaluation, but the effects can be mitigated if the position is known. Random and unsteady inlet distortion are more challenging to compensate and a minimal amount of random inlet distortion is preferred.

The random inlet distortions are primarily mitigated through the flow conditioner and require detailed considerations. The general outline of the flow conditioning is shown in Fig. 4.2 where streamlines coloured by velocity magnitude are seeded from the inlet to illustrate the flow path inside the flow conditioner. The flow enters at the inlet and in the azimuthal direction into the volute. The volute maintains a constant azimuthal velocity while the flow is guided radially through eight HEX. The HEX serves two purposes; first, they keep the thermal balance in the facility as they are connected to the building central cooling system. Second, the HEX reduces non-uniformity in the flow. The cross-section plane and streamlines illustrate the acceleration from radial to the axial direction in the contraction after the HEX. The contours at the outlet plane follow the same colour scale as the streamlines and cross-section contours in Fig. 4.2. The simulation of the flow conditioning unit was performed in STAR-CCM+ and is detailed in Paper E. In Fig. 4.2, the azimuthal variation of total pressure and velocity at midspan 300 mm downstream of the outlet plane is illustrated below the isometric view of the flow conditioner. At the outlet plane at the midspan, the numerical results indicated variations in total pressure and velocity below ± 1% of the mean flow, which was considered sufficient.

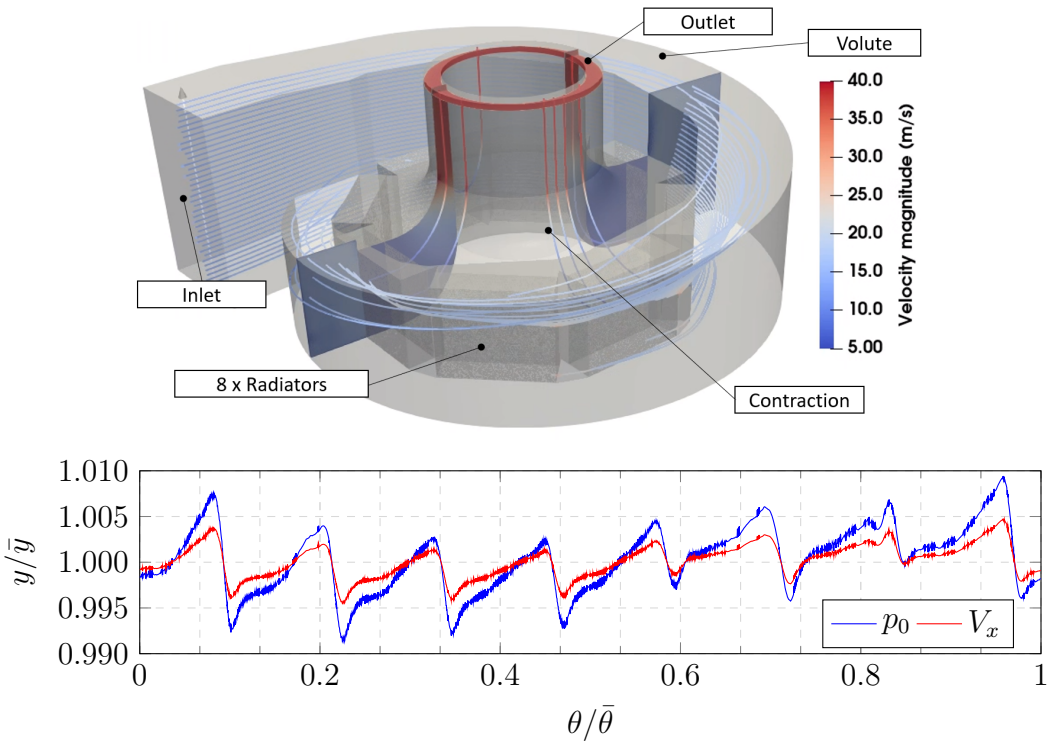

Figure 4.2: Midspan velocity and pressure distribution 300 mm downstream of the contraction outlet (Lower) and the streamlines from the numerical simulation (Upper). Spacing of grid lines on the plot represent tangential resolution for inlet condition probe access.

After the contraction, the flow is guided through a transport channel where it passes by structural struts. The structural struts are shaped as NACA0018 profiles to reduce the wake and placed with a 90-degree offset. After the transport channel, the flow is accelerated in a contraction with a contraction ratio of 0.85. Before entering the IGV, a turbulence screen is placed to increase turbulence levels and further reduce residual non-uniformity.

4.1.2 Design of Low-Pressure Compressor Unit

This section describes the aerodynamic and mechanical design of the low-pressure compressor but begins with the rationale behind some fundamental and practical design parameters.

Reynolds Number

The operation of a compressor in respect to Reynolds numbers can be divided into three regimes. First is the lower (also called laminar separation) regime $Re_{crit,L}$. The name is derived from the often occurring laminar separation on the suction side, causing a rapid loss in performance and turning ability, illustrated to the left in Fig. 4.3. This ranges from 100,000 by Shäffler [46] to as low as 50,000 by Carter [9]. The upper critical region (also called roughness region) is defined by a relation to surface roughness but can, for most aero-engine representative surfaces, be around 600,000 [46]. In this region, polytropic efficiency is nearly Reynolds number independent as surface features penetrate the sub-layer, as illustrated to the right in Fig. 4.3. Between these two regions is where the vast majority of low-speed test rigs operates with, for the most part, an attached turbulent boundary layer. Interoperated in Fig. 4.3 is the polytropic efficiency on the vertical axis and rotor chord Reynolds number on the hotisontal axis. The trends of polytropic efficiency throughout the three regions are illustrated by a black dashed line for typical values and a blue shaded zone that represents relative ranges in the data set for [46, 9]. In the laminar region, one can note a high Reynolds dependency of the polytropic efficiency. Near the interface of $Re_{crit,L}$ there is little correlation to Reynolds numbers as variations between compressors can influence when the flow translates between a laminar separation to turbulent operation. The lowest acceptable operational point at 3×10^6 Re_c was selected to mitigate the aforementioned undesired operational conditions. The horizontal solid red line in Fig. 4.3 represents the facility design operation from a 3×10^6 - 6×10^6 Re_c with the design point at 5.75×10^6. With this selected operational range, speed-lines down to 0.5 should be possible without any risk of large scale laminar separation. The facility is capable of being operational down to even lower Reynolds numbers to be able to identify the $Re_{crit,L}$ with some penalty in measurement accuracy. The lower operation region is shown in Fig. 4.3 as the horizontal red dashed line.

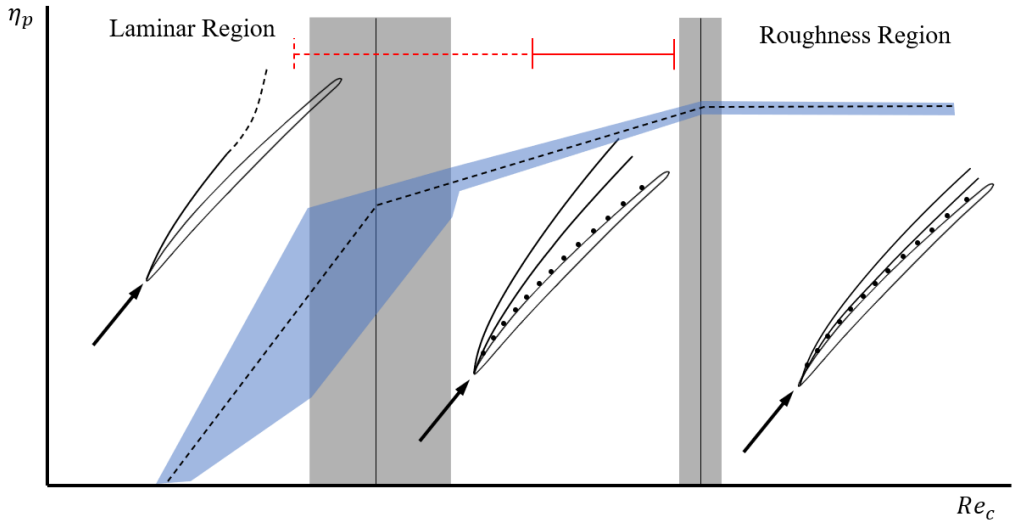

Figure 4.3: Operational regions of a compressor in relation to rotor chord Reynolds number. A schematic boundary layer development relative to surface features for each region together with representative polytropic efficiency (black dashed line), typical ranges in the existing experimental data (blue shaded area) and facility operational range (red horizontal line).

Free-stream Turbulence

Turbulence intensity and length-scale influence the boundary development and are known to influence performance in turbomachinery [33]. Hence, a representative level is important to achieve. However, the turbulence intensity can vary substantially in a compressor, so a specific value is arguably hard to pinpoint. Ranges for low-speed facilities are reported in [8] with ranges from 3-11% between different low-speed test facilities. Data for high-pressure compressor outlets at full speed tests are reported to be in ranges of 6-7% in [19]. Mayle [33] investigated the effect of free-stream turbulence on the critical momentum thickness number at higher Reynolds numbers. His results indicate that the effect from turbulence intensity above 3-4% generally subsidies. Numerical simulations on compressor blades from [58] based on transition models of B. Abu-Ghannam and R. Shaw [1] shown in [47] suggest that at a Reynolds of 5×10^6, any turbulence level above 2-3% should have a small effect on the transition onset location. With this in mind, an isotropic turbulence intensity of $3-4\%$ at the inlet of the IGV was targeted. The turbulence was achieved using a single turbulence grid upstream of the IGV inlet. For the final design, a turbulence grid with 1mm steel wires and a centre gap of 3.15mm was selected to achieve 3.75% turbulence intensity at the IGV inlet during design operation. The selection of the screens and calculation of turbulence decay was performed following guidelines in [20].

An interesting note is that when Schreiber [47] investigated the combined effects of Reynolds and turbulence on transition location in a linear cascade, he observed high sensitivity to both turbulence and Reynolds number at around a Re_c of 200,000 and a turbulence level around 3%. This concurs with earlier presented studies and strengthens the rationale for a lower selected Re_c of 300,000 and a turbulence intensity of $3-4\%$ as this places the facility far upstream of these critical conditions.

Another interesting note is that Cyrus [13] showed that increasing the turbulence from 3.8 to 6.2% moved the stall factor towards a lower flow factor for the same load coefficient. The facility where the experiments were performed is similar in Reynolds number, size and rotational speed as the design at Chalmers Laboratory of Fluids and Thermal Sciences.

It is worth noting that discussing turbulence without consideration for length-scale is a gross oversimplification but is arguably sufficient for initial design and general down-selection.

Surface Roughness Effects

The surface roughness impacts the aerodynamic performance of the LPC. A near hydraulic low surface roughness is performed to avoid effects from surface roughness, but a smoother surface negatively impacts component price. Therefore, a reasonable level of surface roughness level for current operational conditions needs to be defined.

From a fluid dynamic perspective, the geometrical sand-grain roughness k_s, sand-grain roughness height $k_{s,h}$ and the dimensionless friction factor f are commonly used. However, in practice, the surface specifications in technical drawings are statistical, as defined by ISO-4287 [26]. An exact conversion from statistical ISO units such as R_a and R_y to geometrical sand grain roughness k_s is a much-debated subject. In Paper C, a GKN in-house correlation was used to relate statistical values to surface roughness.

For low-speed compressors test facilities, surface roughness typically affects the boundary layer development and separation location. In simplified two-dimensional conditions, the dependency of surface roughness effects on the boundary layer state can be framed by discussing the dimensionless surface roughness k_s^+. This is defined by the equivalent sand-grain roughness divided by the normalised to the viscous boundary layer thickness δ_v as shown in Eq. 4.1.

$$k_s^+ = \frac{k_s}{\delta_v} \quad \underbrace{0 \leq k_s^+ \leq 5}_{Smooth} \quad \underbrace{5 \leq k_s^+ \leq 70}_{Transitional} \quad \underbrace{70 \leq k_s^+}_{Rough} \tag{4.1}$$

The effect of the dimensionless surface roughness can be divided into three zones. Below a value of five k_s^+, the surface can be considered hydraulically smooth. At values with a dimensionless roughness parameter above 70, the surface can be considered fully rough as the average fluctuation penetrates the overlap region. In the area between these two, the surface topology has a significant impact on boundary layer development. In this area, the conversion from statistical to equivalent sand-grain roughness is arguably challenging. One empirical model derived from a relatively large dataset of measured surfaces is presented by Flack and Schultz [18] and is defined in Eq. (4.2). R_q is the RSS of perturbations, and Rsk is the skewness as defined in ISO-4287. The skewness provides a measure of the direction of the surface variations. At a high skewness, the majority of the perturbation extrudes into the flow and vice-versa.

$$k_s = 4.43 R_q (1 + Rsk)^{1.37} \tag{4.2}$$

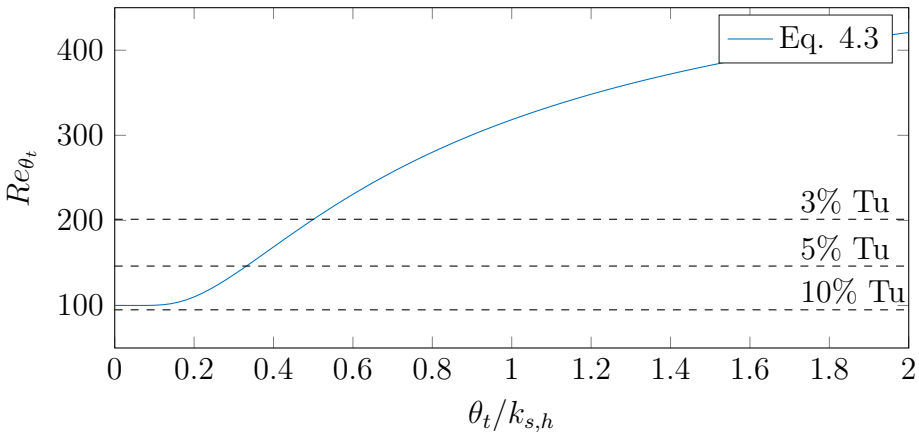

Figure 4.4: Turbulence and surface roughness effects on the transition onset momentum thickness Reynolds number Re_{θ_t}.

Assuming that the measured surface roughness has been estimated correctly, the surface roughness effect on the laminar-turbulent transition onset location can be estimated using the roughness parameter $\theta_t/k_{s,h}$. This parameter has been empirically correlated to the onset momentum thickness Reynolds number by using Eq. (4.3).

$$Re_{\theta_t} = 100 + 0.43e^{(7-0.77\frac{k_{s,h}}{\theta_t})} \tag{4.3}$$

$$Re_{\theta_t} = 400Tu^{5/8} \tag{4.4}$$

Equations (4.3) and (4.4) describe the effect from surface roughness and turbulence levels respectively and both are illustrated in Fig. 4.4. Figure 4.4 shows that for most turbulence levels expected in the LPC (3%-10%), the sand-grain roughness height needs to be in the order of two to five times the size as the momentum thickness θ to make an impact on the momentum thickness at transition onset. This method provides a starting point when defining the manufacturing demands on aero surfaces.

With the presented design, a rotor blade operating around ADP perceives a velocity of $70-80$ m/s and assumed turbulence of 3% at midspan. Equation (4.4) provides an onset momentum thickness Reynolds number, and with ambient conditions, an estimated momentum thickness. Inserting these into Eq. (4.3), the maximum allowed sand grain roughness can then be estimated to $k_s = 16.5\,\mu$m. In a modern, five-axis, high-speed spindle CNC-mill it is relatively easy to achieve a R_q and Rsk that would result in a sand grain roughness below $k_s = 16.5\,\mu$m. After discussion with manufacturers and providing ample margin of error in the above rationale, a $Rq \leq 2\,\mu$m and a near-zero Rsk were targeted. The manufactured blades have a R_q below one and a Rsk near zero along the milling cusps with slightly higher values across the cusps.

In terms of surface roughness and geometrical design, local manufacturing defects are present and accepted near the trailing edge on the pressure side. These defects consist of entry and exit paths from the milling finishing procedure.

Compressibility Effects

All the experimental and numerical work related to this facility was performed at low Mach numbers. In a real engine, the flow is compressible with an ICD inlet Ma-number around $0.4 - 0.6$ and local peaks of $0.8 - 0.9$. Critical features in the ICD are instabilities and stochastic features in the boundary layer, which are challenging to capture numerically and significantly impact heat transfer and duct performance. These features are possible to evaluate at a low Ma-number in otherwise representative conditions.

The last two stages in the LPC are typically transonic, which this facility can not replicate. There are several models [51, 28] to predict the general compressibility effect on an axial compressor. Nevertheless, even if general trends can be predicted with some confidence, it is hard to argue that the specifics of shock interaction with stall mechanics, end-wall mixing and tip leakage can be predicted accurately using simple models [15]. Both [59] and [57] outline design methods applied to scale certain aspects such as blade loading when scaling the high-speed design to lower speed, but neither has a detailed comparison between the two. The rationale from [14] can nevertheless be used to assess areas in which the impact from compressible effects are expected as they scale to the magnitude of Ma number. The Ma number increases with radius and for a typical high-speed LPC, the Ma number is below 1 for span location below ≈50%. Therefore, the most significant discrepancy between high-speed and low-speed cases is expected to be near the shroud.

Tip-Clearance

Tip-clearance primarily affects the secondary flow structures, either by leakage through the tip clearance or by the scraping of the low momentum boundary layer at the shroud [14]. A smaller tip clearance will reduce the leakage but increase the scraping of the boundary layer. Sakulkaew [45] showed that for transonic compressors, there should be a minimum theoretical loss between the competing loss mechanisms at a tip clearance height of $0.1 - 1\%$ ε of the channel height h. Below a span-wise clearance of 0.4 %, [45] and [16] computed similar stage performance with and without tip-clearance. The tip-clearance effects on stall margin are often evaluated by the pitch-line gap g to tip clearance, where values below 0.01 do not affect the stall margin. To allow features caused by both leakage flow and scraping, a tip clearance of 1%, ≈ 0.75 mm or $\varepsilon/g = 0.022$ is selected for the baseline compressor. The tip clearance can be varied locally by in-situ adjustment or for a whole stage by replacement of shroud inserts made of Ureol®. The relatively large tip clearance of 1% of h reduces manufacturing costs on rotor and shroud as a larger throw is acceptable. A sensitivity analysis using the correlations from [28] and [14] provide performance variations in the order of $0.5 - 1\%$ for a throw of $\pm$ 0.075 mm.

Engine Similitude

With the compressor parameters set, the aerodynamic design of the compressor was iterated between the experimentalist (author) and the aerodynamic designer.

The aerodynamic designer generally strives to match the engine similitude with the reference engine, fundamentally limited by the power available. On the other hand, the experimentalist attempts to optimise measurement conditions and reduce manufacturing prices. As a result, the iterative process is rather tedious, with numerous conflicting design demands. The bulk of iterations were performed at Chalmers using in-house tools. With a satisfactory design at Chalmers, a few final design iterations were performed at GKN Aerospace. The aerodynamic design, from zero-dimensional to three-dimensional numerical simulations, follows the practice detailed in [30]. The numerical simulations of the LPC are detailed in Paper F.

One of the most reoccurring touchpoints during the design process was the channel height, and it serves as a good example. A shorter channel height was preferred from an aerodynamic perspective. However, a reduced channel height leads to increased wind speed and rotational speed, increased blockage effects from probes, decreased spanwise probing resolution and decreased blade size, all of which increase manufacturing complexity or limit instrumental access.

The final LPC design at ADP compared to the engine similarities reference engine is shown in Fig.4.5. The variation from the reference compressor of the presented engine similitude is less than 5% for all factors except Reynolds number Re_c and Ma-number.

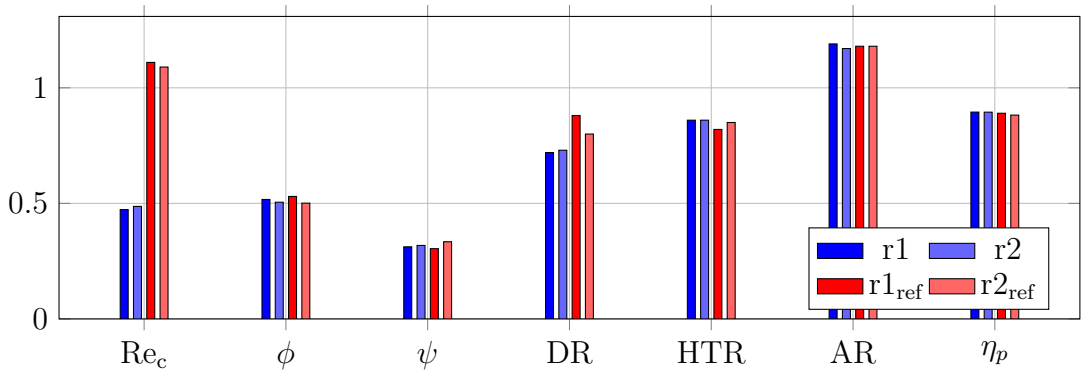

Figure 4.5: Facility compressor parameters in comparison to reference engine parameters. AR – Aspect ratio; HTR - Hub-to-tip ratio; DR – Degree of reaction; Re – Chord based Reynolds number; ϕ – Flow coefficient; ψ – Stage loading; η_p – Polytropic efficiency.

Rotor Mechanical Design

The mechanical design of the rotor is not the primary target of this thesis, but as it directly impacted the aero design, a summary of the design procedure is provided in this section. The target of the mechanical design was to ensure the rotor's mechanical integrity. Since most of the simulations could not be verified before manufacturing, a conservative safety factor was targeted, and designs were selected that allowed post-hoc failure mode mitigations. This summary contains some aspects of little academic value but can be helpful for future users of the facility and rig designers.

The rotor assembly is designed with two independent discs for each rotor row and is mounted in an overhang configuration with most of the rotating mass extended

outside two bearings. The two-disc configuration is not the mechanically optimal design and is seldom used in commercial engines, where rotors mounted on a drum supported on each side is often preferred. The concept implemented was a trade-off to maximise access and versatility of the facility. The large overhang mass was possible due to the vertical configuration of the facility where loads from gravity are axisymmetrically distributed. The lack of a bearing downstream of the compressor allowed the OGV and ICD to be designed without consideration for mechanical load transfer from a rotor bearing, which greatly enhanced access and modularity. The two-disc configuration has lower hub leakage compared to a drum and was substantially more cost-effective.

A multitude of solutions to manufacturing the rotor blades was iterated, where the final candidate was an aluminium CNC blade with an isosceles trapezoid (UK definition) mount. This mount provided a reasonable balance between manufacturability, price and stress distribution.

The mechanical integrity of the rotor was ensured by first addressing the static loads and later transient loads. The rotor is exposed to periodic loads and necessitates structural simulations assessing fatigue failure. A maximum operational time of 5000 hours in 8-hour intervals was selected as this would cover the facility running at all times from the set inauguration date to the end of the project. A gross overestimation of the dynamic load was selected by assuming that the blade would perceive the highest simulated load at each wake passage. With 124 stators at 1920 RPM for 5000 hours, this leads to a single rotor blade perceiving 7.2×10^9 cycles. The confidence of cycle fatigue load generally decreases with the number of cycles, primarily due to the dependency of environmental effects, the quality of the surface and any internal impurity to initialise the first crack.

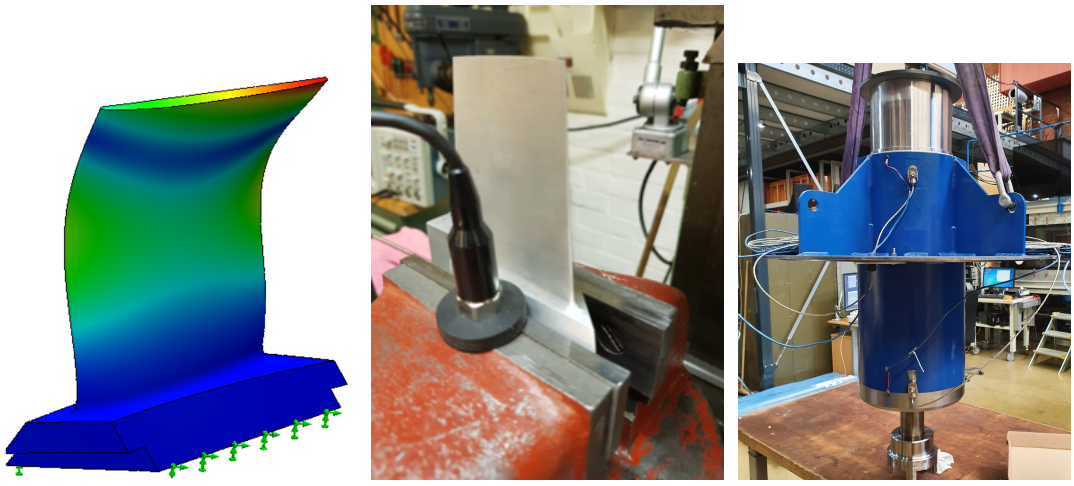

(a) (b) (c)

Figure 4.6: (a) Mode 3 of CooperV2 R1 simulation; (b) single blade ping test of the as machined CooperV2 R1 geometry; and (c) the assembly with rotor housing before mounted in the facility.

The mechanical integrity of the rotors was relatively straightforward, while the modal simulation of the two rotor blades impacted the aero design. Several

complete redesigns were required to mitigate excitation modes near or precisely at the operational range. The modal simulation was verified by a ping test on manufacturing samples together with the department of structural dynamics at Chalmers. The ping set-up is shown in Fig. 4.6b where the blade is mounted only in the lower edges in the wise. The test matched the third mode at 2709 Hz shown in Fig. 4.6a of a dynamic structural simulation within 1.2% difference. As a side note, the number of blades was changed from 60 in early versions to 61 (prime) to mitigate divisors near the excitation frequency.

A rotor housing was designed to allow for machining the bearing seats in one process (mitigates issues with bearing alignment), contain all rotor monitoring instrumentation and allow for shaft mounting outside the facility. The rotor housing substantially simplified assembly and is shown in Fig. 4.6c.

4.1.3 Design of Intermediate Compressor Duct

This section describes the general design of the intermediate compressor duct. The baseline aero designed was performed at GKN and is beyond the scope of this thesis. The design of the ICD was targeted to be a more aggressive design in terms of radial reduction relative to the length of the duct, $\Delta R/L$. The aim was to stress critical parts of the duct without large-scale separation. An aggressive duct provides a reasonable starting point for design attempts to shorten the duct with hex integration. Representative values of ICD design parameters such as inlet channel height to duct length h/L and inlet and outlet area ratio A_o/A_i were sought and guided the compressor's design.

Dimensioning

Table 4.1 shows fundamental design parameters and typical values for three different design domains, the selected baseline design and open access geometry of the VINK compressor presented in [30]. Fundamental design parameters are the relative radial variation of duct length $\Delta R/L$, inlet channel height to duct length h_i/L, the outlet area relative to the inlet area A_o/A_i and the loss coefficient, which is the total pressure losses relative to inlet total pressure $Y_p = P_t - P_{t,in}/q_r ef$ as defined in [36]. Very aggressive ducts are defined as ducts with large-scale hub separations and total pressure losses of $Y_p \geq 0.1$. Aggressive is defined as ducts with small or limited separations and losses in the order of $Y_p \approx 0.1 - 0.05$. Conventional ducts are defined where little or no separations occur $Y_p \leq 0.05$. Note that the ranges of the three design domains, very aggressive, aggressive and conventional, are arbitrarily derived from figures, results and tables in [36, 35, 54] by the author of this thesis. The study of Ortiz Duenas [36] was largely used to categorise the duct designs based on pressure loss coefficient Y_p. Duenas studied a duct representative of a modern S-duct with a $\Delta R/L = 0.5$ where no separations occurred. A re-optimised duct with $\Delta R/L = 0.67$ increased losses slightly while a optimised duct with $\Delta R/L = 0.78$ had a rapid increase in losses due to large-scale hub separation.

Throughout the facility's design, a relative high channel heigh was sought due to the many benefits such a configuration brings to most probing instrumentation.

Table 4.1: Table of ICD design ranges from very aggressive to conventional together with selected design for the ICD and the open geometry of the VINK compressor.

	Very Aggressive	Aggressive	Conv. [36]	Baseline	VINK
$\Delta R/L$	0.6-0.9	0.6	0.5	0.64	0.41
h/L	0.15-0.3*	0.15-0.3*	0.15-0.3*	0.43	0.6
A_o/A_i	0.8-1*	0.9-1.15*	1	0.99	1.15
Y_p	≥ 0.1	$\approx 0.1 - 0.05$	$\leq 0.01 - 0.05$	0.06	-

*Estimated from figures in publications [35, 36, 54, 55].

Due to geometrical constraints, several feasible configurations within the LPC design space were not possible within the ICD design space. The limitation can be derived from the targeted area ratio of $A_o/A_i = 1$, the targeted LPC radius $R_{1,mid}$ together with a high ratio of duct turning to inlet midspan radius $\Delta R/R_{1,mid}$. Combinations occurred where the geometrical hub radius at the outlet was below zero.

From the definition in Table 4.1, one may note that the baseline design can be categorized in the aggressive to a very aggressive domain with losses in the order of $0.05 \leq Y_p \leq 0.1$.

Design and Aerodynamic Simulations

With a selected feasible design target, the final aero-design was provided by GKN and simulated at Charmers as part of the LPC simulation in Sec. 4.1.2 using Ansys^{TM} CFX 2019 R1 with the turbulence model $k - \omega$ SST, mixing plane and enhanced wall functions. Details of the numerical simulation are also presented in Paper 5.

Construction of the ICD

The versatility and access of the ICD was considered crucial as more design iterations of the ICD are expected compared to other components such as OGV or LPC. A few design choices were essential to achieve a versatile ICD module. The vertical design and the upstream flow restrictor allow the ICD to be placed open-ended to ambient air; this permits access from all directions for both instrumentation and personnel. To further mitigate design limitations inflicted from other subsystems, the ICD module is separated from traverses, instrumentation and other structures such as the OGVs. The benefit of separating the modules apart allows the ICD to be rapidly replaced with minimal modifications as the aero surfaces in the ICD only interferes with a facility by few contact surfaces and a few bolts to fasten the module axially. Furthermore, the OGVs, hub, shroud and struts in the ICD-module can be individually replaced.

The final design of the baseline configuration of the ICD mounted in the facility is shown in Fig. 4.7, containing colour-coded components that represent the different access types and locations. Red indicates the traverse system for ICD volume access, blue for the LPC outlet's traverse access, yellow for traverse and optical access within the LPC, and the green represents radial access within the LPC. Key components

are marked in Fig. 4.7 such as rotor and stator blades, probe access and other instrumentation, some of which are described below. Fig. 4.7 shows the boundaries B_A to B_C; these are described with the rationale for instrumentation configuration later in this work.

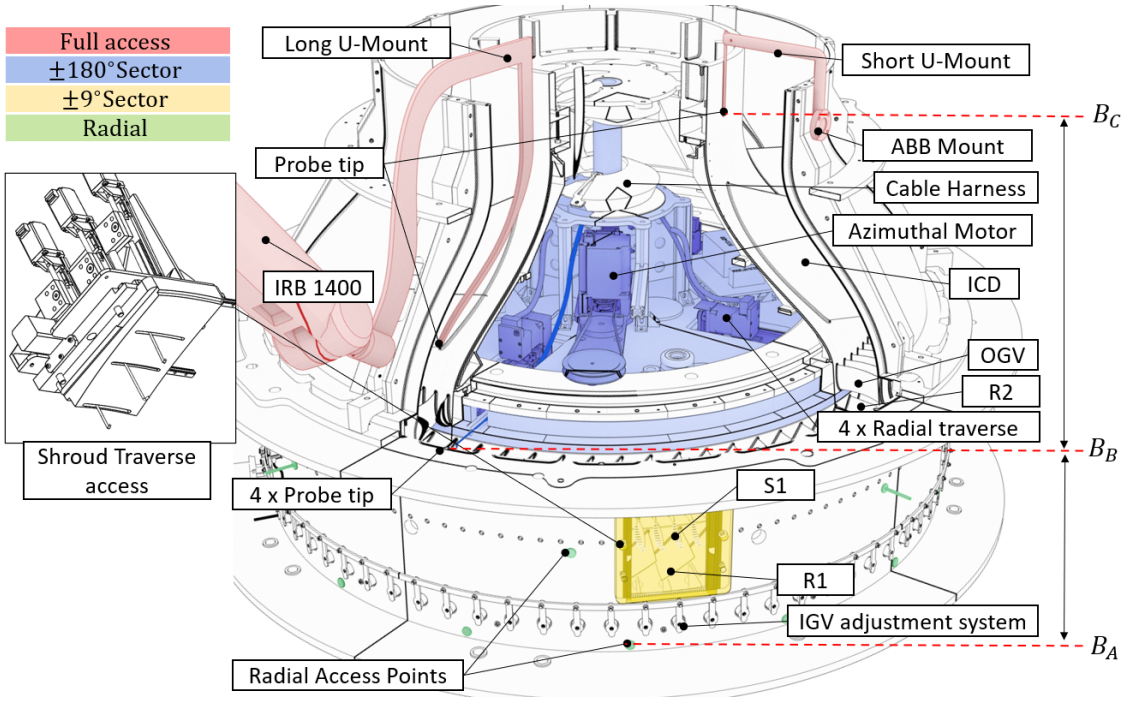

Figure 4.7: Schematic illustration of the baseline ICD instrumentation, traverses mounted on the LPC unit. See text for further information.

More than fulfilling the aerodynamic purpose of the OGV, the OGV module provides mechanical support through the gas path for the hub-mounted traverse module and ICD. The OGVs can also be instrumented or substituted, either as individual blades or as one of the fourteen modules of nine OGVs.

A hub-mounted traverse system was selected as it allows for easy 360-degree access upstream of the OGV without penetrating the LPC containment. The already present axial gap between the LPC and the OGV allows for relatively relaxed manufacturing tolerances, and the interface could be machined relatively cost-effectively. A similar hub-mounted traverse downstream of the OGV was neglected as in this access location any protrusion at the hub downstream of the OGVs could potentially have a significant effect on the turning ability of the duct.

Several designs of traverse access through the ICD shroud were attempted for the outlet and intermediate planes in the ICD. However, a robotic arm was found to be the more cost-effective and versatile traversing equipment to access the ICD domain, as little to no modification would be required between each ICD iteration. Shroud mounted traverses are expected to be used in some ICD configurations but will be part of the ICD specific instrumentation and assembled outside the facility.

Traverse Details

The final design uses an ABB RBK-1400 shown in Fig. 4.7. The position accuracy of a robotic arm is inversely proportional to the distance of the mounting point, and the distance from the downstream outlet to the OGV outlet is around 400 mm. No robot on the market was identified that could position the probe tip within suitable tolerances if the probe tip distance to the mounting point was 400 mm. A U-probe has been designed, which mitigates the need to penetrate the shroud and still have low position uncertainty in the probe location. This configuration is suitable for low-speed applications where probe blockage has a limited upstream effect, and forces on the probe holder are relatively low. The hub-mounted traverse system includes four radial traverses designs based on Nanotec PD2-C4118L1804-E-01 and Misumi LX2001P-MX-B1-F-200. Each traverse system shares the same mounting point and can move individually. The whole traverse assembly rotates tangentially where the load transfer to rotate the traverse system is by an inverse T3 timing belt set-up. The timing belt is glued inside the HepcoMotion R-76-799-r360 ring, and a T3 timing pulley is mounted on the rotating traverse. A Nanotec PD6-C8918S6404-E-09 with a gear ratio of 31:1 by two belt reductions provides the motion control to the T3 timing. The internal diameter of the HepcoMotion ring is not dividable to an even number of T3 teeth, and the missing pulley was replaced with a mechanical stop. Therefore, the traverse system cannot provide true 360-degrees access for an individual probe since it is missing roughly 0.5°. There are four individual traverses, so 360-degree access is still true for the system. The 31:1 gear ratio between the motor and the T3 pulley was required to provide sufficiently high tangential resolution. Furthermore, the large Nanotec PD6 stepper motor was selected to handle aerodynamic loads on the traverse system from the second LPC rotor and the four probes inserted into the highly swirling LPC outlet air. The traverse system is fully exposed to the LPC rotor with only 1-5mm axial distance. The mechanical stop inside the HepcoMotion R-76-799-r360 ring hinders free rotation of the traverse system if braking power of the Nanotec PD6 motor is lost.

4.2 Instrumentation

The instrumentation was central throughout the iterative design of the facility. Design choices were ultimately evaluated from an instrumentation perspective by assessing the expected measurement quality with various fidelity, from simple MCS of the subsystem to a extensive pre-test evaluation as presented in Paper F. The instrumentation and control systems were organised in a hierarchy of modules with mapped out evaluation chains, which provides an overseeable perspective of the instrumentation and is shown in Fig. 4.8. For example, most of the procedures described in sector. 3.3.1 are represented by the box named MHP.

The information flow is illustrated as solid arrows where the thick arrows are network communication between the modules. Subsystems within each module are marked with white background italic text, such as the ABB ACS250-800 motor controller, shown as ABB or the inlet mass-flow controller shown as $\dot{m}$ in the

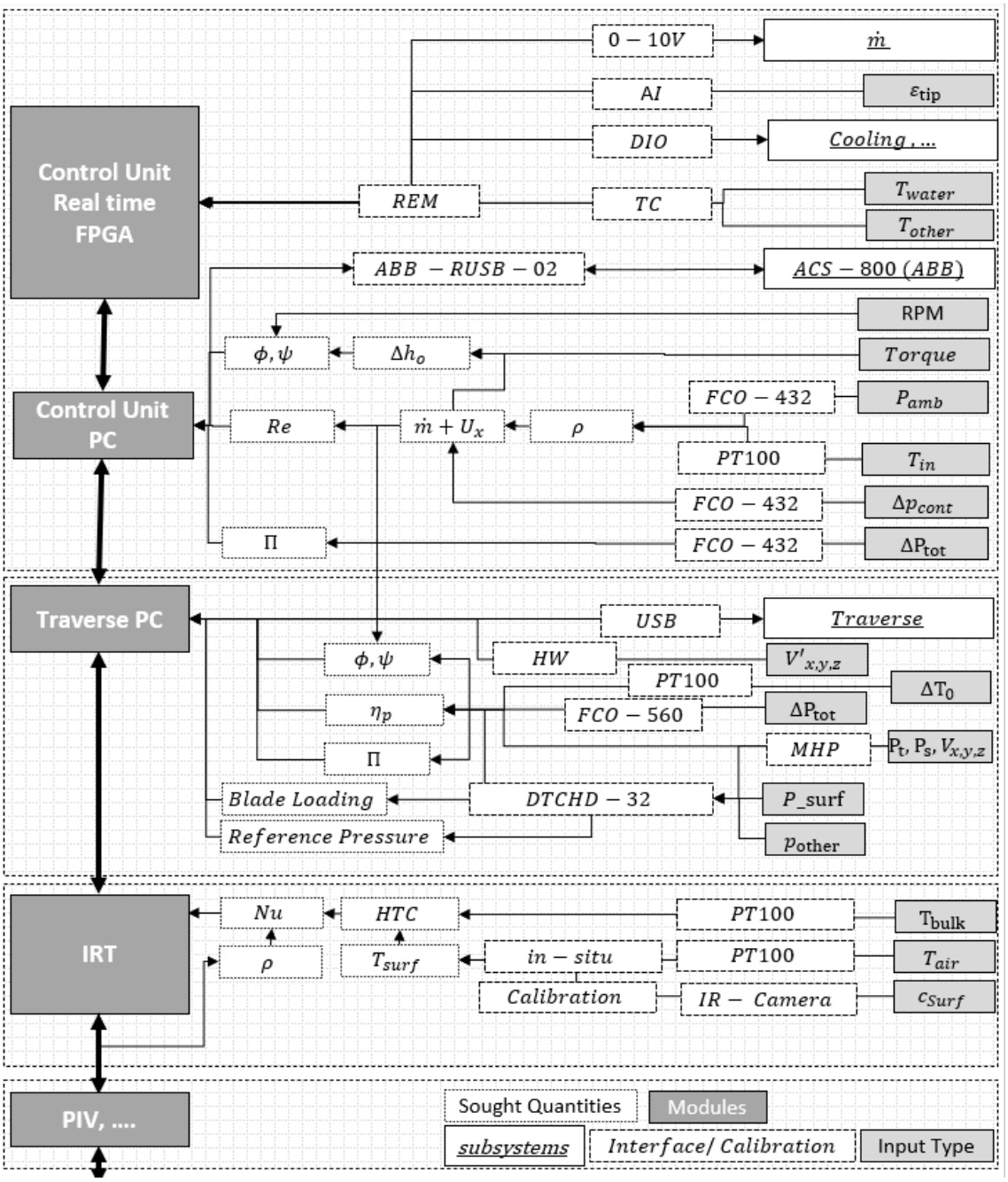

Figure 4.8: Flowchart of signals, data processing and sampling devices for different modules in the facility.

schematics. The boxes with the white background and dotted border are input variables used to calculate sought quantities. One can notice redundancies of measured quantities for one sought quantity, for example, the load coefficient ϕ. For monitoring, the load coefficient is derived from mass flow and shaft input power. This is suitable for monitoring purposes due to the direct sampling time, but it is unsuitable for performance evaluation at this facility, as shown in Paper F. For performance evaluation, the same coefficient is calculated from gas-path studies in the traverse

module. The same is true for pressure ratio, which is calculated using static probes for monitoring but by gas-path studies for the performance evaluation. The flowchart also shows some of the measurement pathways; RPM can be derived from both the ABB motor controller and the rotational trigger on the shaft.

The central part of the facility is the control unit, which ensures the facility's safe operation. Other modules are added to expand the instrumentation. The monitoring module is running on a PC using LabView™ and a RealTime module NI-9504. The build-in FPGA in the NI-9504 performs low-level analysis on accelerometer and high-speed voltage signals such as rotor encoder and tip-clearance monitoring. The NI-9504 digital and analogue interfaces are expanded using the National instruments REM series. These REM modules have a relatively slow update rate and are therefore only suitable for monitoring and control of $\dot{m}$ and cooling system logic. The traversing module with internal modules for data acquisition such as multi-hole probe set-up as described in Chapter 3.3 or hot-wire anemometry as described in Papers A, D and E. Another separated module is PIV and heat transfer and laminar-turbulent transition investigation by IR-thermography. The IR-thermography method is described in 3.3, attached Papers C and D and some implementation in the ICD in Sec. 4.2. The individual modules communicate to the facility primary over a local network, digital port for low-level communication and TTL signals for more time-sensitive triggers.

4.2.1 Pneumatic Measurements

The pneumatic instrumentation in the LPC and ICD is similar to the TRS. Pneumatic probes, both single and multi-hole, are in the ICD and LPC of different sizes and manufacturing methods compared to what is used in the LPC, but the method is the same. The detailed explanation of pneumatic measurement described in Chapter 3.3 using experimental data from the TRS test facility is, in large part, valid for measurements in the LPC-ICD test facility. The pneumatic probes in the LPC-ICD test facility are manufacturing using high precision binder jetting by DigitalMetal® AB and calibrated in the Chalmers in-house calibrator. A 1.8 mm diameter Kiel probe, a 2.8 mm diameter Prandtl probe and 5HP manufactured by DigitalMetal® AB are shown in Fig. 4.9.

Paper F details an uncertainty assessment of the pneumatic probe measurement in the LPC. To clarify the experimental set-up, Fig. 4.8 shows the general outline of the information flow in the LPC and ICD with details of the pneumatic and temperature measurement devices. Figure 4.8 illustrates the core unit with access location and the configuration of investigating boundary B_A, B_B and B_C by probing and pressure taps on the strut. Following the flow direction, the first pneumatic measurements are in the contraction, where an FCO-432 measures the differential static pressure over the contraction. The solid black line illustrates the positive reading port, and red represents the negative and is henceforth referred to as the reference port. The grey boxes outlined with solid black lines are solid-fluid interfaces where the pressure is measured. Each interface requires detailed consideration but is ignored on a system-level. The MHP boxes are, for example, covered by most of Chapter 3.3 while the Kiel probe is considered in Paper F. The FCO-432 provides a

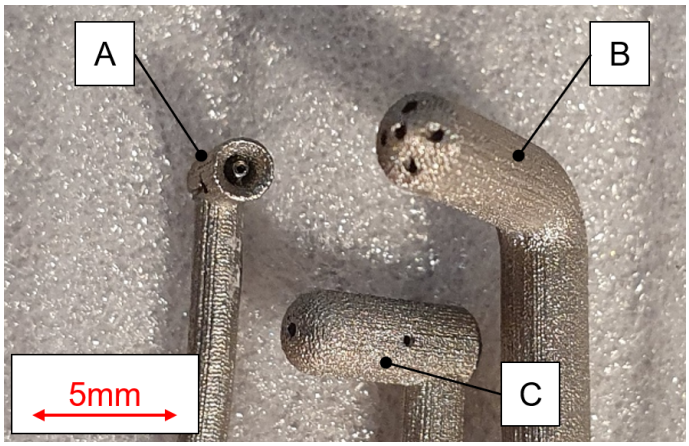

Figure 4.9: Pneumatic probes for baseline instrumentation in inside the LPC and ICD manufactured by DigitalMetal® AB, (A – Kiel probe, B – 5HP, C – Prandtl probe).

cost-effective and stable single-channel measurement and is easily calibrated against the FCO-560 micro manometer. Downstream of the contraction, Kiel and Prantle probes are inserted into the flow. All Kiel probes in the LPC and ICD are identical with an outer diameter of 1.8 mm. The inlet Kiel probe is differentially connected by the FCO-560 to the statically mounted Kiel probe at boundary B_B. There are two Kiel probes at boundary B_B, one used for total pressure normalisation and one for pressure rise Π in the LPC. The inlet is accessed by inserting a probe radially through the shroud via 10 mm diameter holes. Radial inlet total pressure, velocity and static pressure profiles are gathered by radially traversing a Prantl probe through the 10mm hole. The Prantl probe is differentially connected to another Prantl probe permanently mounted at boundary A at another tangential position for normalisation. The measurement is repeated at several azimuthal locations around boundary A to provide inlet profile variations along the inlet. All pneumatic pressure measurements in the LPC and ICD are gatherer by two ESP-32HD units referenced to the statically mounted Kiel probe at boundary B_B. Pressure measurements inside the LPC, such as static blade pressure or pneumatic probes mounted on the 18° traverse system, utilise an ESP-32HD with piping through the shroud. A second ESP-32HD, located inside the ICD, is used for all the pneumatic measurements in the gas path of the ICD with the Run Ref connected to the same statically mounted Kiel probe at B_B. The pressure tap implementation on the strut and shroud is near identical to the TRS with pressure taps printed in SLA vanes and hubs as described in [42].

4.2.2 Temperature and Heat Transfer Measurements

Figure 4.10 includes the basic set-up for the temperature measurements in the LPC and ICD following the same schematic indication as in Fig. 4.8. Following the flow direction, the temperature is measured at the inlet boundary B_A using three PT-100 delivered from Pentronic. The PT-100 is shielded in a SLA manufactured mount to mitigate shunt offset and static temperature offset. Identical probes are used for all stagnation temperature measurements. At B_B and B_C one sensor is

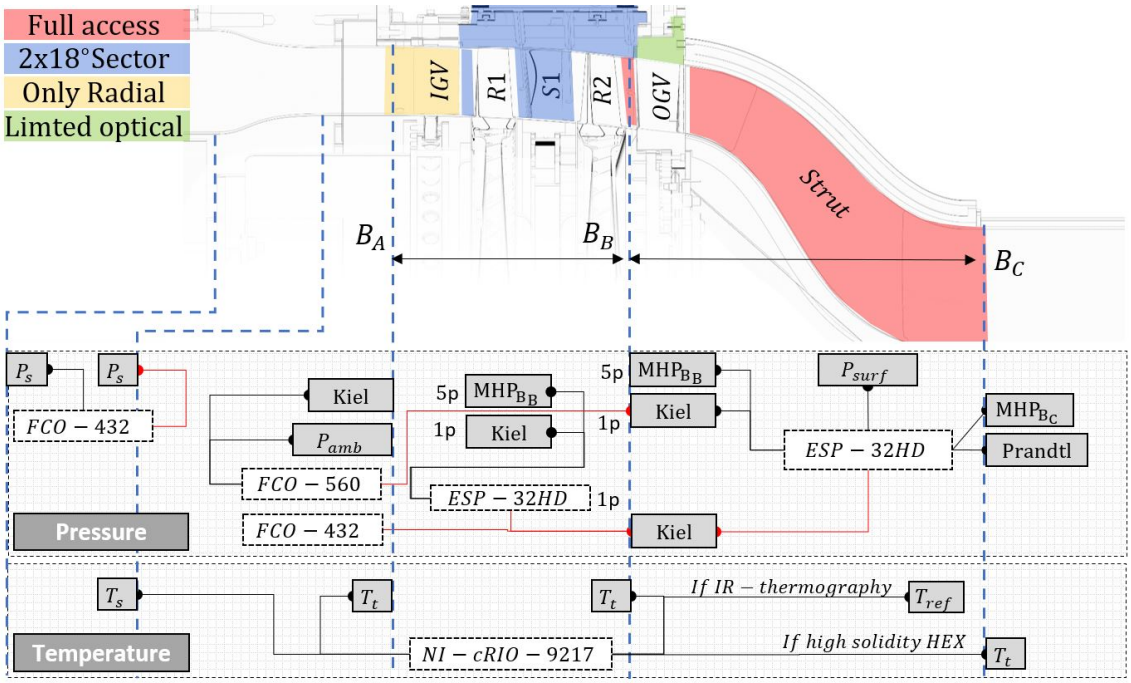

Figure 4.10: Flowchart of signals and instrumentation location in the LPC and ICD.

permanently mounted while the other is mounted on the traverse system. The PT-100 probes between interface B_A and B_B are used to evaluate LPC baseline performance during ICD studies. The Pentronic PT-100 RTD elements are accreditated down to uncertainty of 0.02 K. The NI-9127 used to sample the RTD temperatures in the LPC and ICD can provide this resolution but with a device bias offset device of ±0.1 K.

Chapter 3.3 and Paper C describe the implementation of IR-thermography to measure convective heat transfer coefficient and detect the laminar-turbulent transition in the TRS module. The ICD is designed to accommodate the same method on strut, hub and shroud. Optical access is granted to the hub and most of the strut without penetrating the hub or shroud line. Reflectors, mirrors or drilled holes will provide optical access to the leading edge and potentially to the shroud. A schematic of an instrumented hub segment manufactured by additive manufacturing is illustrated in Fig. 4.11. The water is pumped into the lower collector box, pushed out into the channel, and collected in the outlet collector before exiting the test section. Using this set-up hinders high-quality heat transfer measurement near the very start and end of the ICD hub line. The current setup hinders high-quality heat transfer measurement near the start and end of the ICD hub line due to high uncertainty in the inner wall heat transfer rate. However, the area is heated, so transition or separation will be possible to detect.

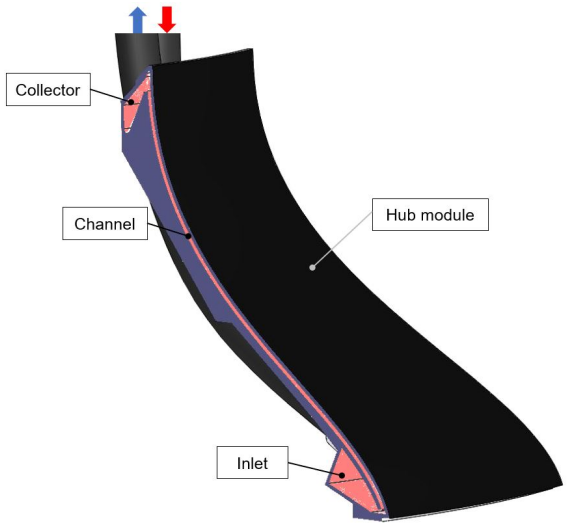

Figure 4.11: Hub segment for heat transfer measurements in the ICD with water entering at the inlet and exiting at the collector, and the black surface is in contact with the coreflow in the ICD.

4.3 Pre-test Evaluation of Low-Pressure Compressor

Before final manufacturing, the instrumentation in the LPC was evaluated by a pre-study using the numerical results from the CFD of the LPC and ICD presented earlier in this work. The pre-study was performed by virtually performing all the expected steps during an experimental test campaign to find issues and devise potential mitigations before the final design was commissioned for manufacturing. This section provides a general description of the detailed pre-study in Paper F and provides some examples and expansions of description based on feedback from peers.

The TRS module in the LPT-OGV test facility is experimentally similar to the ICD, and we generally understood how to measure the aerothermal performance of such a module. However, in the lab, we had limited experience of measuring the compressor performance, namely, pressure ratio, Π, efficiency η_c and normalised mass flow $\dot{m}_{corr}$. The target was to measure these with a maximum error of 1% and Paper F describes the processes to achieve this target. In formulating this target, measuring mass flow with an accuracy of 1% in a large-scale facility is challenging. However, mass-flow measurements can be performed outside the compressor unit, and future work could be dedicated to address this issue. Furthermore, to avoid errors from mass flow measurement propagating into other compressor performance parameters, these need to be isolated from the mass flow measurements. In doing so, efficiency cannot be measured by any means such as shaft power [1] or thermal balance of the system as these require mass flow as a variable input. Since the instrumentation to measure flow properties by traversing was already required for flow field investigations, the idea is to utilise these further to calculate the performance of the compressor. The

[1]Shaft power further introduces a number of challenges with bearing and viscous losses not related to compressor performance.

foremost challenge in measuring the performance of an 80-91% efficient LPC is the low temperature difference between the inlet and outlet of the compressor. To accurately capture this temperature difference, great care is needed.

Performing a pre-test evaluation on the numerical flow field early on instead of the experimental flow field is beneficial as design changes in digital geometry are practically free when compared to modifying already manufactured components. There are some limitations when using the numerical flow field; the flow field is modelled and will, for many reasons, not perfectly reflect the final experimental flow field. However, there are somewhat less apparent benefits of using numerical results for these kinds of studies where the predominant ones are the controlled environment and simple integration of the flow field. The controlled and stable environment allows for features to be evaluated individually, something that might be impossible or very time consuming to perform experimentally. For example, paper F investigates the required traverse mesh density to capture the average flow values within a targeted accuracy. Numerically it is relativity simple to interpolate a boundary with variable mesh density until a satisfactory difference to boundary average is achieved. If the numerical flow field is representative, the study provide critical information and specification to the instrumentation such as resolution and maximum allowed probe size. The same mesh study is required to be performed with experimental data but these are are available at the design stage and will be influenced by operational fluctuations, measurement errors and instrumentation limitations.From the pre-study performed on the LPC, dominant error sources could be divided into four groups, single-point accuracy, discretisation error, data normalisation and error propagation. A brief description of these is given below:

Single point accuracy is the measurement error at a point. Assuming a probing acquisition, there are several reasons the probe reading value is not accurate. The transducer introduces noise, later the probe does not read the actual value, and the probe itself interferes with the flow field. In short, the transducer error was addressed by acquiring the best transducers on the market and minimising the reading range to the absolute smallest allowed, which in this case, is differential between the inlet and outlet. A probe might be mis-reading the value in the flow as too high gradients over the probe area or other interference with the probing port. The ratio of a probe reading and real fluid properties is often referred to as the recovery factor. One mitigatigation of the effect from the recovery factors when performing differential measurements is to use identical probes in similar flow fields since the offset is similar at both locations. The axial location of the compressor outlet evaluation plane was adjusted to maximise similarity to the inlet plane sole due to this. The influence of the probe on the flow field was not investigated. The relatively low-speed nature of the facility and small probes leads the author to expect minimal effects from blockage on the reading on the probe but was not further investigated.

Traverse discretisation error is the difference between the actual mean flow properties and a discrete sampling of the flow. By interactively increasing the mesh density, a sufficient cover ratio is identified. As a note from the performed

pre-study in Paper F, the author believes it is improbable that rakes of 8-10 points as recommended in PTC 19.5 are sufficient to gather gas properties within 1% error in most applications.

Data Normalisation is briefly presented in Paper F but is based on normalising of one static reference scaled to data gathered by traversing. The data normalisation in Paper F has been expanded in section 2.5.2 based on requests from peers.

Error Propagation With single point measurement and discretisation uncertainties estimated, the final error, including data normalisation, is estimated using error propagations as described in Section 2.5.1. Details of each subsystem and the process are provided in Paper F.

The final uncertainty for test configurations optimised for measuring the isentropic efficiency of the compressor is shown in Fig. 4.12 where Π is the stage loading, $\dot{m}$ the mass flow and η_{is} the isentropic efficiency. On the vertical axis, the errors are given as a percentage, and the different colours indicate the contribution for the different error source and the total estimated error source. The total pressure ratio can mainly be limited by the FCO-560 accuracy and discretisation (blue) and normalisation (orange) have little effect. As mentioned before, it is challenging to achieve mass flow measurement uncertainty below 1% due to the discharge coefficient, reflected in Fig.4.12. Uncertainties of isentropic efficiency below 0.5 % are shown in Paper F and Fig.4.12, where the main contributor is the differential temperature measurements.

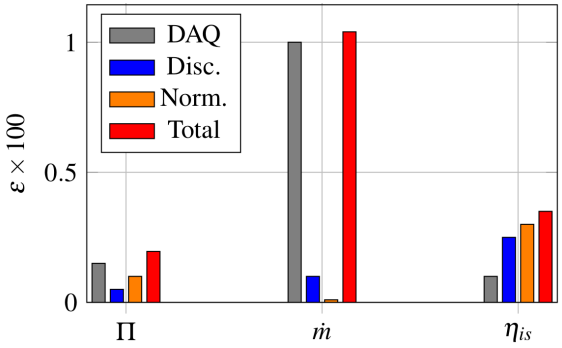

Figure 4.12: The bar diagram showing estimated uncertainties of the stage loading mass flow $\dot{m}$ and isentropic efficiency η_{is} with the total uncertainty shown as red, discretisation as blue, normalisation as orange and single point acquisition as grey.

The author would like to comment that even though the study in Paper F shows promising results and provides insights arguably impossible to achieve with experimental studies, the uncertainty analysis was performed on numerical data. Thus, error sources are certainly overlooked, and unknown issues are to be expected when experimentally implemented. However, with an error estimation indicating a less than 0.5% uncertainty, it is arguably likely that an error below 1% should be achievable if it is properly experimentally implemented.

Chapter 5

Summary of Papers

Paper A

Division of Work

Besides being the main author, my main contribution is the experimental implementation and analysis. The co-authors provided feedback on the paper and analysis of the results.

Summary and Discussion

This paper presents novel results of surface roughness and Reynolds number effect on the losses in the TRS. Three different levels of roughness are applied and tested at design conditions at two different Reynolds numbers. The two surface roughnesses with the lowest Ra are in the range of what would be reasonable to assume in a TRS module during real engine operation. Since the effect from the surface roughness was unknown at the start of the experiment, a sample with very high surface roughness $Ra \approx 30$ was added to emphasise the effect of surface roughness variation. Turbulence decay and pressure-based boundary layer measurements were performed. Suction side flow features were documented via flow visualisation.

As two Reynolds numbers were evaluated, the Reynolds number effect could be seen for both a smooth hydraulic vane as well as rough surfaces. Flow visualisation also showed the secondary flow structure and estimated transition/separation area along the suction side.

The experimental results determine typical surface roughness influence on pressure losses and wake with an increased surface roughness causing an increased wake width and losses along the whole OGV span. The effect was the same for the two first smoother coatings at higher Reynolds numbers, but a substantial increase of losses was revealed around the suction side near the hub for the roughest surface.

Contribution

The paper presents novel results from roughness effects in an annular TRS module. The paper provides reference values for numerical studies regarding turbulence decay,

Reynolds number effects and roughness effects. Moreover, flow visualisation and boundary layer measurement identifies critical areas for further experimental studies.

Paper B

Division of Work

As a second author of this paper, I primarily provided experimental data and analysis and feedback on the numerical findings presented. Shrikanth Deshpande performed the numerical study and the writing. Valery Chernoray provided feedback on the findings and writing.

Summary and Discussion

The paper describes a complementary numerical analysis of the experimental study performed in Paper A using steady-state RANS simulations with a correlation-based transition SST model ($\gamma - \theta$). Since no information about the fboundary layer momentum thickness at the transition location was known, the default settings of the transition model were used.

Contribution

Both wake studies and blade loadings are used to compare numerical and experimental data with good agreement. In general, the numerical results overpredicted the losses and underestimated the unpredictable the relative increase in losses with increased surface roughness.

Paper C

Division of Work

Apart from being the main author, I provided conceptualisation, measurement and data analysis. Valery Chernoray contributed with conceptualisation and feedback on findings and Radeeshe Dhanasegaran provided support with experimental measurement and writing.

Summary and Discussion

This paper primarily describes the uncertainty estimation and mitigation for steady-state heat transfer when implemented on an OGV in the TRS. The paper provides heat transfer coefficient result on a OGV at a Reynolds number of 235,000 for three different load cases. The heat transfer coefficient distribution reveals the same flow features from flow visualisation performed in Paper A with a similar-sized roll-up and transition/separation location.

Contribution

The paper presents the first heat transfer measurement on a TRS at engine-representative conditions. Additionally, an accurate and relatively simple implementation of heat transfer studies was presented. The method has few geometrical limitations and is suitable for heat transfer studies in other applications. The paper is not a complete implementation guide but shows aspects of mitigating uncertainness typically found in this kind of studies.

Paper D

Division of Work

Besides being the main author, I provided the experimental analysis and results. Boundary layer measurement using hot-wire was provided from a dataset of unpublished work by Valentin Vikhorev. Srikanth Deshpande performed the numerical studies while Jonas Larsson and Oskar Thulin contributed valuable analysis and support in writing. Valery Chernoray provided general feedback and helped with data sampling of the hot-wire measurement.

Summary and Discussion

The paper primarily covers three aspects. Firstly, it discusses in detail the usage of IR-thermography for full-span laminar-turbulent transition measurement on the suction side. Secondly, the transition modelling on a hydraulicly smooth vane is studied and compared in detail at midspan transition location and across the whole span. Finally, fundamental laminar-turbulent transition correlations are compared to experimental and numerical findings.

Contribution

The paper provides experimental results of transition location of the whole span for three different load cases and verifies the detection of transition location by IR-thermography in the TRS. The paper also provides insight into potential reasons for the difference between the numerical and experimental data and the existing experimental correlation.

Paper E

Division of Work

Besides being the main author, I was the head designer of the facility described in the paper. The aero design of the LPC was performed in collaboration with Carlos Xisto and Marcus Lejon. The final aero design of the LPC was done at GKN but simulated at Chalmers. The flow conditioning unit was simulated by Debarshee Ghosh. Tomas

Grönstedt provided input and general feedback throughout the facility design and writing of the paper.

Summary and Discussion

The paper covers the general design of the facility together with more detailed information about a selection of the facility components such as flow conditioning and details of the ICD instrumentation. The paper describes the basics of the challenges of measuring the performance of the LPC by gas-path studies and shows a simplified uncertainty estimation of the proposed instrumentation. The paper indicates that it is possible to measure compressor performance with better than 1% accuracy except for normalised mass-flow.

Contribution

The work provides insight into the design and challenges of designing the low-speed compressor facility and compiles essential design considerations for later facility designers or facility users. The paper also explores instrumentation challenges and that highly accurate compressor performance evaluation is possible using gas-path studies for low-speed, highly efficient low-pressure compressor facilities.

Paper F

Division of Work

Besides being the main author, I was the head designer of the facility described in the paper and performed the extensive pre-test evaluation. The aero design of the LPC was conducted in collaboration with Carlos Xisto and Marcus Lejon creating the numerical simulations. The final areo design of the LPC was done at GKN but simulated at Chalmers. Anders Dahl aided in the design and construction of the facility. Tomas Grönstedt provided general feedback and aided throughout the work with writing conceptualisation.

Summary and Discussion

The paper describes the pre-test evaluation performed for future aerothermal studies of the LPC using the flow field from numerical simulations. The pre-test evaluation concurs with earlier approximated estimated uncertainties in measurements of the LPC performance but adds details of individual error sources and mitigations. The paper also further describes the numerical simulations used in the pre-test evaluation.

Contribution

The paper primary provides a pre-test evaluation of the compressor performance by using gas-path studies. The configuration and set-up strongly indicate that the

compressor performance parameters should be possible to sample with an uncertainty better than 1% with the exception of the mass-flow. Results from numerical simulations of the low-speed compressor are presented for the first time.

Paper G

Division of Work

Besides being the the first author, I was part of the design and provided input and designs for numerical simulations. Carlos Xisto performed the simulations and Tomas Grönstedt and Marcus Lejon aided with general input in the design and writing process.

Summary and Discussion

The paper introduces a radical vane-integrated heat exchanger in the ICD with potential gains and design challenges. It first presents an aggressively designed duct with separation occurring along with the hub. Next, two design iterations are introduced where a splitter vane is placed in the flow to increase the wetted surface for heat transfer and suppress the hub separation. The first design iteration completely suppresses the hub separation but have splitter and shroud separations instead. The second design iteration reduces the separations in general but introduces an early separation at the hub.

Contribution

The paper contributes an increased understanding of the potential and design challenges of radical vane-integrated heat exchanger in the ICD, but further design work is required to produce a viable design.

Chapter 6

Concluding Remarks

This thesis has addressed the challenge to experimentally evaluate the aerothermal performance on internal jet engine structures. Some lessons learned, findings and concluding remarks are presented in the following paragraphs.

Multi-hole probe The multi-hole probe is an attractive measurement technique for academic and industrial applications due to its robustness and ability to measure the flow pressure, angles and velocities at probe tip. The technique is more than half a century old, but new aspects of its implementation are constantly being developed. This work addressed the fundamental and practical challenges of implementing the multi-hole probe for performance measurements in low-speed testing of the internal jet engine structure TRS. The thesis shows that with the current data reduction, the main contributor to the uncertainty is the error introduced from the pressure transducers. It presents a method to reduce the errors introduced when measuring the total pressure in the TRS by changing the pressure reference for the pressure transducers. This change of reference results in an uncertainty reduction of 50% in total pressure measurement in the TRS. This relatively simple modification of a well-established method was identified due to the presented detailed uncertainty analysis of the probe implementation at Chalmers. There is a slight penalty in the reference change but only at cone angles not present in the measurement planes of the TRS. The approach is easily adapted for other implementations, but potential benefits depend on the sought quantity and test conditions.

Convective heat transfer measurments To perform aerothermal studies of the internal jet engine components, measurements of the convective heat transfer on the aero surfaces were required. Generally, convective heat transfer measurements have high uncertainty levels, and even for simple fundamental verification cases, the uncertainty presented is rarely better than $5 - 15\%$. This work describes the implementation of heat transfer measurements on an OGV in a TRS module using a water heated core and solving the conjugate heat transfer with an assessed uncertainty of 4-6%. A comprehensive uncertainty analysis supports the assessed uncertainty. The analysis has been performed iteratively to remove dominant uncertainties by re-engineering the measurement chain. The analysis still has a few known unknowns, but

these could largely be mitigated during testing. Furthermore, the test geometry was manufactured by additive manufacturing, and the method can easily be implemented for other studies.

Transition detection using IR-thermography IR-thermography in combination with other measurement methods is a well-known method to detect laminar-turbulent transition or separation location. The detection using IR-thermography has been verified using boundary layer hot-wire measurements at selected locations in the TRS and provides important validation data for the aerodynamic designer.

Aerothermal performance of the TRS This thesis presents results related to a baseline OGV with a relatively comprehensive experimental data set with transition location, surface heat transfer, aerodynamic performance, turbulence decay, wake structures and insights of the secondary flow structures at representative engine conditions. The results are of great interest for the TRS designer and contribute to the limited publically available results on the aerodynamic and aerothermal performance of TRS at engine representative conditions.

Design and construction of a new low-speed compressor facility for aerothermal investigations A new compressor facility has been constructed to enable detailed and accurate aerothermal measurement of intermediate compressor ducts. At the time of writing, the results from the facility are not ready for publication as all subsystems are not yet functional. Therefore, the thesis has focused on design choices, instrumentation and construction. The facility is designed from fundamental design demands such as surface roughness effect and suitable operational Reynolds numbers to an operational low-pressure compressor of 4000+ parts. The thesis presents the fundamental design aspects of the LPC, which might seem superfluous, but I find it intriguing that the equivalent of a facility specification sheet is often presented in a short paragraph or appears to be provided without discussion. I assure the reader that the facility's design demands have been debated thoroughly and updated to mitigate design demands when possible.

Isentropic efficiency of a low-speed LPC A substantial part of the design of the compressor facility was to ensure that sought quantities could be measured with sufficient accuracy. One critical and challenging parameter was the compressor efficiency. Most of the PTC standard performance measurement procedures such as shaft power and total pressure rakes were evaluated but were for various reasons ill-suited for low-speed performance measurement. Typically, one of the required quantities to calculate efficiencies such as mass flow or losses from shaft to the gas path was challenging to achieve with better than 1% in bias error. Uncertainties tend to increase when concepts are taken into real-world practice, and fully relying on a technique that has a lower estimated uncertainty than 1% could be problematic. Evaluation of the compressor by the isentropic efficiency mitigates all significant bias errors but instead requires accurate measurement of specific enthalpy and entropy changes between two boundaries. The limiting factor for low-speed applications is

often a minuscule temperature difference and operational stability. By undertaking a detailed pre-test evaluation and designing the facility to enable highly accurate isentropic efficiency measurements, an uncertainty of better than 0.5% seems plausible. This is a reasonable starting point for an expected measured near or below 1%, which is currently being pursued. Instrumentation to perform shaft input power measurements and rake measurements are included in the facility set-up.

Bibliography

[1] B. J. Abu-Ghannam and R. Shaw. "Natural Transition of Boundary Layers—The Effects of Turbulence, Pressure Gradient, and Flow History". In: *Journal of Mechanical Engineering Science* 22.5 (1980), pp. 213–228.

[2] ASME ASME International. *Test Uncertainty PTC 19.1.* Tech. rep. ASME International ASME, 2005.

[3] Lars-Uno Axelsson. *Experimental investigation of the flow field in an aggressive intermediate turbine duct.* Doktorsavhandling vid Chalmers tekniska högskola Ny serie: 2945. Chalmers University of Technology. ISBN: 9789173852647.

[4] D. W. Bailey et al. "Performance Assessment of an Annular S-Shaped Duct". In: *Journal of Turbomachinery* 119.1 (Jan. 1997), pp. 149–156.

[5] J.B. Barlow, W.H. Rae, and A. Pope. *Low-Speed Wind Tunnel Testing.* Aerospace engineering, mechanical engineering. Wiley, 1999. ISBN: 9780471557746.

[6] P. Bradshaw and R.C. Pankhurst. "The design of low-speed wind tunnels". In: *Progress in Aerospace Sciences* 5 (1964), pp. 1–69. ISSN: 0376-0421.

[7] K.M. Britchford et al. "Measurement and prediction of low in annular S-shaped ducts". In: *Experimental Thermal and Fluid Science* 9.2 (1994). Special Issue on Measurement in Turbulent Flow, pp. 197–205. ISSN: 0894-1777.

[8] T. R. Camp and H.-W. Shin. "Turbulence Intensity and Length Scale Measurements in Multistage Compressors". In: *Journal of Turbomachinery* 117.1 (Jan. 1995), pp. 38–46. ISSN: 0889-504X. DOI: 10.1115/1.2835642.

[9] ADS Carter et al. *The effect of Reynolds number on the performance of a single-stage compressor.* Ministry of Aviation, Aeronautical Research Council, 1957.

[10] Shaowen Chen et al. "Numerical Study of the Air Bleeding Caused Non-Uniformity in Axial Compressor". In: *Journal of Thermal Science* 29 (Mar. 2019).

[11] Valery Chernoray and Johan Hjärne. "Improving the Accuracy of Multihole Probe Measurements in Velocity Gradients". In: 2 (Jan. 2008).

[12] James Crawford and A Michael Birk. "Improvements to common data reduction and calibration methods for seven hole probes". In: *Journal of fluids engineering* 135.3 (2013).

[13] Vaclav Cyrus. "An Experimental Study of Stall in Four Axial Compressor Stages". In: vol. Volume 1 Aircraft Engine Marine Turbomachinery Microturbines and Small Turbomachinery. Turbo Expo Power for Land, Sea, and Air. May 2000. DOI: 10.1115/2000-GT-0504.

[14] J. D. Denton. "The 1993 IGTI Scholar Lecture: Loss Mechanisms in Turbomachines". In: *Journal of Turbomachinery* 115.4 (Oct. 1993), pp. 621–656. ISSN: 0889-504X. DOI: 10.1115/1.2929299.

[15] John D. Denton. "Some Limitations of Turbomachinery CFD". In: vol. Volume 7: Turbomachinery, Parts A, B, and C. Turbo Expo: Power for Land, Sea, and Air. June 2010, pp. 735–745. DOI: 10.1115/GT2010-22540.

[16] Lars Ellbrant, Lars-Erik Eriksson, and Hans Mårtensson. "Predictive Capability of CFD Models for Transonic Compressor Design". In: vol. 2B. Turbo Expo. Power for Land, Sea, and Air. June 2014.

[17] K. N. Everett, A. A. Gerner, and D. A. Durston. "Seven-hole cone probes for high angle flow measurement Theory and calibration". In: *AIAA Journal* 21.7 (1983), pp. 992–998.

[18] Karen A. Flack and Michael P. Schultz. "Review of Hydraulic Roughness Scales in the Fully Rough Regime". In: *Journal of Fluids Engineering* 132.4 (Apr. 2010). ISSN: 0098-2202.

[19] H. P. Grant. "Turbulence characteristics of compressor discharge flows. JT9D engine tests". In: vol. 19790016824. NASA. Lewis Res. Center Premixed Prevaporized Combustor Technol. Forum. Jan. 1979, pp. -.

[20] J. Groth and A. V. Johansson. "Turbulence reduction by screens". In: *Journal of Fluid Mechanics* 197 (1988), pp. 139–155.

[21] N. W. Harvey. "Some Effects of Non-Axisymmetric End Wall Profiling on Axial Flow Compressor Aerodynamics: Part I—Linear Cascade Investigation". In: vol. Volume 6: Turbomachinery, Parts A, B, and C. Turbo Expo: Power for Land, Sea, and Air. June 2008, pp. 543–555.

[22] Johan Hjärne, Valery Chernoray, and Jonas Larsson. "Experimental Investigations and Numerical Validation of an Outlet Guide Vane With an Engine Mount Recess". In: *Proc. of ASME Turbo Expo 2008*. June 2008, pp. 989–998.

[23] Johan Hjärne, Valery Chernoray, Jonas Larsson, et al. "Numerical validations of secondary flows and loss development downstream of a highly loaded low pressure turbine outlet guide vane cascade". In: *Proc. of ASME Turbo Expo 2007*. 2007, pp. 723–733.

[24] Johan Hjärne, Jonas Larsson, and Lennart Lofdahl. "Performance and Off-Design Characteristics for Low Pressure Turbine Outlet Guide Vanes: Measurements and Calculations". In: *Proc. of ASME Turbo Expo 2006*. Vol. Volume 6: Turbomachinery, Parts A and B. May 2006, pp. 649–658.

[25] ISO International Organization for Standardization. *General requirements for the competence of testing and calibration laboratories, 17025*. Tech. rep. International Organization for Standardization, 2008.

[26] ISO International Organization for Standardization. *Geometrical Product Specifications (GPS) — Surface texture, 4287*. Tech. rep. International Organization for Standardization, 1997.

[27] B. Kirollos and T. Povey. "High-accuracy infra-red thermography method using reflective marker arrays". In: *Measurement Science and Technology* 28.9 (2017), p. 095405.

[28] C. C. Koch. "Stalling Pressure Rise Capability of Axial Flow Compressor Stages". In: *Journal of Engineering for Power* 103.4 (Oct. 1981), pp. 645–656. ISSN: 0022-0825. DOI: 10.1115/1.3230787.

[29] H.H. Ku. "Notes on the use of propagation of error formulas". In: *Journal of Research of the National Bureau of Standards* 70C.4 (1966), p. 263.

[30] Marcus Lejon et al. "Multidisciplinary design of a three stage high speed booster". In: *Turbo Expo: Power for Land, Sea, and Air*. Vol. 50794. ASME. 2017, V02BT41A037.

[31] J. P. Longley. "Measured and Predicted Effects of Inlet Distortion on Axial Compressors". In: vol. Volume 1: Turbomachinery. Turbo Expo: Power for Land, Sea, and Air. V001T01A067. June 1990. DOI: 10.1115/90-GT-214.

[32] Andreas Marn et al. "Comparison of the Aerodynamics of Acoustically Designed EGVs and a State-of-the-Art EGV". In: 45608 (2014).

[33] Robert Edward Mayle. "The 1991 IGTI Scholar Lecture: The Role of Laminar-Turbulent Transition in Gas Turbine Engines". In: *Journal of Turbomachinery* 113.4 (Oct. 1991), pp. 509–536. ISSN: 0889-504X.

[34] F. R. Menter et al. "A Correlation-Based Transition Model Using Local Variables—Part I: Model Formulation". In: *Journal of Turbomachinery* 128.3 (Mar. 2004), pp. 413–422.

[35] Edward M. J. Naylor et al. "Optimization of Nonaxisymmetric Endwalls in Compressor S-Shaped Ducts". In: *Journal of Turbomachinery* 132.1 (Sept. 2009). ISSN: 0889-504X. DOI: 10.1115/1.3103927.

[36] C. Ortiz Duen~as et al. "Effect of Length on Compressor Inter-Stage Duct Performance". In: vol. Volume 6: Turbo Expo 2007, Parts A and B. Turbo Expo: Power for Land, Sea, and Air. May 2007, pp. 319–329. DOI: 10.1115/GT2007-27752.

[37] T. J. Praisner and J. P. Clark. "Predicting Transition in Turbomachinery—Part I: A Review and New Model Development". In: *Journal of Turbomachinery* 129.1 (Mar. 2004), pp. 1–13.

[38] M. Raffel and Christoph B. Merz. "Differential infrared thermography for unsteady boundary-layer transition measurements". In: *AIAA journal* 52.9 (2014), pp. 2090–2093.

[39] V. Ramakrishnan and O. Rediniotis. "Calibration and Data-Reduction Algorithms for Nonconventional Multihole Pressure Probes". In: *Aiaa Journal - AIAA J* 43 (May 2005), pp. 941–952.

[40] Kai Richter et al. “Boundary layer transition characteristics of a full-scale helicopter rotor in hover”. In: *AHS 72nd Annual Forum*. 2016, pp. 17–19.

[41] Kai Richter et al. “Detection of Unsteady Boundary Layer Transition Using Three Experimental Methods”. In: Jan. 2016.

[42] Borja Rojo. “Aerothermal Experimental Investigation of LPT-OGVs”. PhD Thesis. Gothenburg: Chalmers University of Technology, 2017.

[43] Borja Rojo, Carlos Jimenez, and Valery Chernoray. “Experimental Heat Transfer Study of Endwall in a Linear Cascade with IR Thermography”. In: *EPJ Web of Conferences* 67 (Feb. 2014).

[44] Reuven Y. Rubinstein and Dirk P. Kroese. *Simulation and the Monte Carlo method*. Wiley series in probability and statistics. John Wiley & Sons, 2017. ISBN: 9781118632161.

[45] S. Sakulkaew et al. “Compressor efficiency variation with rotor tip gap from vanishing to large clearance”. In: *Journal of turbomachinery* 135.3 (2013).

[46] A. Schaffler. “Experimental and Analytical Investigation of the Effects of Reynolds Number and Blade Surface Roughness on Multistage Axial Flow Compressors”. In: *Journal of Engineering for Power* 102.1 (Jan. 1980), pp. 5–12.

[47] H. Schreiber, W. Steinert, and B. Kusters. “Effects of Reynolds Number and Free-Stream Turbulence on Boundary Layer Transition in a Compressor Cascade ”. In: *Journal of Turbomachinery* 124.1 (Feb. 2000), pp. 1–9. ISSN: 0889-504X. DOI: 10.1115/1.1413471.

[48] C. A. Scribner. “The Effect of Turbulence Intensity and Reynolds Number on the Aerodynamic Behaviour of Kiel, Three-Hole, and Seven-Hole Pressure Probes”. MA thesis. 1125 Colonel By Dr, Ottawa, ON K1S 5B6, Kanada: Carleton Universityn, 2011.

[49] Elias M. V. Siggeirsson, Niklas Andersson, and Markus Burak Olander. “Numerical and Experimental Aerodynamic Investigation of an S-Shaped Intermediate Compressor Duct With Bleed”. In: *Journal of Turbomachinery* 143.10 (May 2021). 101003. ISSN: 0889-504X. DOI: 10.1115/1.4050670.

[50] Loris Simonassi et al. “On the influence of an acoustically optimized turbine exit casing onto the unsteady flow field downstream of a low pressure turbine rotor”. In: *Journal of Turbomachinery* 141.4 (2019), p. 041003.

[51] W. C. Swan. “A Practical Method of Predicting Transonic-Compressor Performance”. In: *Journal of Engineering for Power* 83.3 (July 1961), pp. 322–330. ISSN: 0022-0825. DOI: 10.1115/1.3673194.

[52] Cameron Tropea and Alexander L Yarin. *Springer handbook of experimental fluid mechanics*. Springer Science & Business Media, 2007.

[53] A. D. Walker, A. G. Barker, and J. F. Carrotte. "Numerical Design and Experimental Evaluation of an Aggressive S-Shaped Compressor Transition Duct With Bleed". In: vol. Volume 7: Turbomachinery, Parts A, B, and C. Turbo Expo: Power for Land, Sea, and Air. June 2011, pp. 151–161.

[54] A. D. Walker et al. "Integrated Outlet Guide Vane Design for an Aggressive S-Shaped Compressor Transition Duct". In: *Journal of Turbomachinery* 135.1 (Oct. 2012). 011035. ISSN: 0889-504X. DOI: 10.1115/1.4006331.

[55] Duncan Walker et al. "Aerodesign and validation of turning struts for an intermediate compressor duct". In: International Society for Air Breathing Engines, Jan. 2015.

[56] Chenglong Wang et al. "An experimental study of heat transfer on an outlet guide vane". In: *ASME Turbo Expo 2014: Turbine Technical Conference and Exposition*. American Society of Mechanical Engineers Digital Collection. 2014.

[57] D. C. Wisler. "Loss Reduction in Axial-Flow Compressors Through Low-Speed Model Testing". In: *Journal of Engineering for Gas Turbines and Power* 107.2 (Apr. 1985), pp. 354–363. ISSN: 0742-4795. DOI: 10.1115/1.3239730.

[58] Harold Youngren and Mark Drela. "Viscous inviscid method for preliminary design of transonic cascades". In: *27th Joint Propulsion Conference*. 1991, p. 2364.

[59] Chenkai Zhang et al. "Three-dimensional compressor blading design improvements in low-speed model testing". In: *Aerospace Science and Technology* 63 (2017), pp. 179–190. ISSN: 1270-9638. DOI: https://doi.org/10.1016/j.ast.2016.12.033.